Scanning Quantum Cryogenic Atom Microscope

Fan Yang, Alicia J. Kollár, Stephen F. Taylor, Richard W. Turner, and Benjamin L. Lev
Departments of Physics and Applied Physics and Ginzton Laboratory, Stanford University, Stanford, California 94305, USA

(Received 19 October 2016; revised manuscript received 10 January 2017; published 27 March 2017)

Microscopic imaging of local magnetic fields provides a window into the organizing principles of complex and technologically relevant condensed-matter materials. However, a wide variety of intriguing strongly correlated and topologically nontrivial materials exhibit poorly understood phenomena outside the detection capability of state-of-the-art high-sensitivity high-resolution scanning probe magnetometers. We introduce a quantum-noise-limited scanning probe magnetometer that can operate from room-to-cryogenic temperatures with unprecedented dc-field sensitivity and micron-scale resolution. The Scanning Quantum Cryogenic Atom Microscope (SQCRAMscope) employs a magnetically levitated atomic Bose-Einstein condensate (BEC), thereby providing immunity to conductive and blackbody radiative heating. The SQCRAMscope has a field sensitivity of 1.4 nT per resolution-limited point (approximately 2 μm) or 6 nT/$\sqrt{\text{Hz}}$ per point at its duty cycle. Compared to point-by-point sensors, the long length of the BEC provides a naturally parallel measurement, allowing one to measure nearly 100 points with an effective field sensitivity of 600 pT/$\sqrt{\text{Hz}}$ for each point during the same time as a point-by-point scanner measures these points sequentially. Moreover, it has a noise floor of 300 pT and provides nearly 2 orders of magnitude improvement in magnetic flux sensitivity (down to 10^{-6} $\Phi_0/\sqrt{\text{Hz}}$) over previous atomic probe magnetometers capable of scanning near samples. These capabilities are carefully benchmarked by imaging magnetic fields arising from microfabricated wire patterns in a system where samples may be scanned, cryogenically cooled, and easily exchanged. We anticipate the SQCRAMscope will provide charge-transport images at temperatures from room temperature to 4 K in unconventional superconductors and topologically nontrivial materials.

DOI: 10.1103/PhysRevApplied.7.034026

I. INTRODUCTION

Quantum sensors comprised of nitrogen-vacancy (NV) color centers in diamond have joined scanning superconducting quantum-interference devices (SQUIDs) in advancing high-sensitivity magnetometry into the nanoscale regime [1–3]. Bose-Einstein condensates (BECs) have also been used for magnetometry [4–8]. We add to this quantum metrology toolbox a carefully calibrated cryogenic scanning magnetometer that exploits the extreme sensitivity of these quantum gases to external fields. The SQCRAMscope operating principle is sketched in Fig. 1. Inhomogeneous magnetic fields from a nearby source exert a Zeeman force on atoms Bose condensed in a smoothly varying harmonic trap. The atoms move in response, distorting the otherwise smooth wave function of the BEC. The BEC density is then imaged by recording the absorption of resonant light using a CCD camera. The local density may be related to field through the BEC equation of state. A 2D-field map is created by raster scanning the relative position of the BEC and the source with a duty cycle limited by the time needed to recreate the BEC after the destructive absorption imaging process. Assuming no z dependence of the source, application of the Biot-Savart law, conservation of current, and a measurement of the distance d between the BEC and sample allows one to convert an $\hat{x}$-$\hat{y}$ map of the $\hat{x}$ field component into a 2D map of the current flow (or magnetic domains) in the source [4–8].

The BEC is confined in a high-aspect-ratio cigar-shaped trap formed using an atom-chip-based magnetic microtrap [9,10] (see Appendix A). This quasi-1D Bose gas lies within the quasicondensate regime because the transverse trap frequency $\omega_\perp$ is 157× larger than the longitudinal trap frequency $\omega_\parallel$, the chemical potential μ is similar in magnitude to $\omega_\perp$, and the gas temperature is 2.6× lower than $\omega_\perp$. As such, density fluctuations are suppressed below the quantum shot-noise limit [11–13], enhancing the field sensitivity (see Appendix C). The equation of state in the quasicondensate regime we employ is given by $\mu_{1\text{D}}(x) = \mu - V(x) = \hbar\omega_\perp\sqrt{1 + 4an_{1\text{D}}(x)}$, where a is the 3D s-wave scattering length, $n_{1\text{D}}(x)$ is the line density, and $V(x)$ is the total potential [14]. This potential is the sum of the well-characterized trapping potential and the magnetic potential $V_m(x)$ to be measured. For the employed atomic state and at the small fields that are measured, the magnetic potential is linearly proportional to field, i.e., $V_m(x) = \mu_B B_x(x)$. Small inhomogeneous fields primarily perturb the trap potential only along the weakly trapped

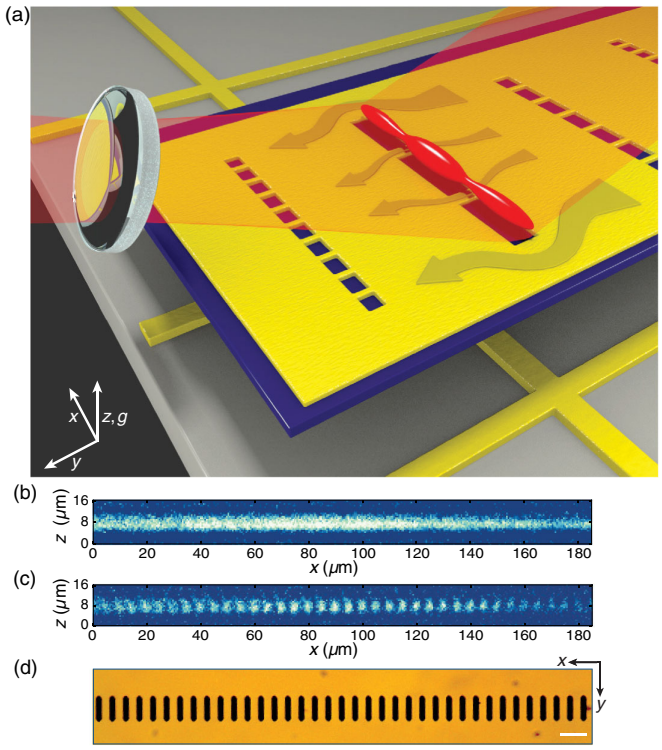

FIG. 1. SQCRAMscope operation. (a) A quasi-1D BEC (red) is magnetically confined using an atom-chip trap (light gray with gold wires). Suspended between the atom chip and the BEC is the silicon sample substrate (blue) onto which the gold calibration pattern is fabricated. The gaps in this gold define the microwires, and the magnetic field from current flowing through these wires (yellow arrows) fragments the BEC. Contact leads not shown. Atomic density is imaged with a high-NA lens by reflecting a resonant laser (transparent red) off the gold. BEC position is fixed while the sample substrate, not connected to the atom chip, may be scanned and cryogenically cooled. For clarity, the sketch is upside down with respect to gravity. (b) Absorption image of an unfragmented quasi-1D BEC at a position $d = 0.8(1)$ μm from the sample. (No current flows.) (c) Absorption image of fragmented BEC. Current flows through periodic array of 2.5-μm-wide wires spaced 2.5 μm apart. (d) Image of the microwire array used in panels (b) and (c). White scale bar is 10 μm.

axis $\hat{x}$ because $\omega_{\parallel} \ll \omega_{\perp}$. Thus, the atomic position can move only a minuscule amount in response to weak transverse fields. Imaging perturbations to the BEC density along $\hat{x}$, therefore, provide a measurement of a vector component of the magnetic potential along $\hat{x}$. The spatial density modulation is measured by absorption imaging with a resonant laser at an intensity well above saturation and reflected at a shallow angle from the reflective sample surface. Much care is taken to account for the presence of the standing-wave intensity pattern of the reflecting beam. See Appendix B.

The responsivity of the magnetometer is given by $\partial n_{1D}/\partial B = \mu_B^2 B/2a\hbar^2\omega_{\perp}^2$. In the limit of low atom number, the equation of state can be approximated by $\mu - V(x) = 2\hbar\omega_{\perp} a n_{1D}(x)$, and the responsivity becomes $R = \mu_B/U_{1D}$, where U_{1D} is the effective 1D-interaction strength $2\hbar\omega_{\perp} a$. We employ two different traps in this work, one whose trap frequencies are optimized for high sensitivity and the other for extended dynamic range.

In the following, we benchmark a number of the SQCRAMscope's attributes. These include (1) the responsivity R [nT/(atom/μm)] of the atomic density to magnetic field variations. (2) The field sensitivity (minimum detectable field). This is quoted in several forms depending on operation modality: field sensitivity (nanoteslas) in a single-shot per resolution-limited point size (RLP), field sensitivity (nT/$\sqrt{\text{Hz}}$) per RLP, and field sensitivity (nT/$\sqrt{\text{Hz}}$) over a finite scan area (to be explained below). (3) Magnetic flux sensitivity ($\Phi_0/\sqrt{\text{Hz}}$) both per RLP and over a finite scan area, where Φ_0 is the magnetic flux quantum. (4) The magnetic field noise floor (in picoteslas) via Allan deviation measurements, which determines the minimum detectable field provided by averaging. (5) Spatial resolutions (in micrometers) of both the field at the BEC and the current in the sample a distance d away. These resolutions are given according to the Rayleigh criterion, which determines the RLP. (6) Current-density resolution (in nanoamperes per micron), which is the current density resolvable by measuring the field a distance d from the surface. (7) The accuracy (in percent), which measures the ability to determine a known field within a certain percentage error. (8) The repeatability (in nanotelsas) quantifies the ability to measure the same field in successive runs and is defined as the average standard deviation in the data. (9) The dynamic range (plus or minus nanoteslas) is the range in field in which the sensor has a linear response R.

To determine these specifications, several other quantities require careful calibrations, including the absorption imaging magnification, the BEC-to-surface distance d, the per-pixel photon shot noise at our CCD camera, the atomic density noise per pixel, and contributions from patch fields. Information regarding these are reported in the appendixes, along with details of the BEC production, the calibration sample, imaging theory, and cryogenic scan results.

The SQCRAMscope enables the high-sensitivity study of strongly correlated and topologically nontrivial materials in unexplored regimes of high temperature and low frequency. For example, the domain structure and transport near twin boundary interfaces in underdoped Fe-arsinide superconductors can be explored as the $T_N \simeq 50$–150 K nematic transition is crossed [16]. Other unconventional superconductors and complex oxide interfaces (e.g., LAO/STO) [17] may be explored at high temperatures, as well as the metal-to-insulator transition in VO_2 [18]. Both transport and static magnetization at the $\gtrsim$100-K ferromagnetic metallic and antiferromagnetic insulating transition in colossal magnetoresistive systems may be imaged. Investigations of topologically protected transport should be possible [19,20], as should investigation of the

electronic hydrodynamic flow in graphene above LN_2 temperatures [21]. Lastly, the SQCRAMscope will also find use in engineering hybrid quantum systems, in coupling BECs to photonic topological metamaterials, and in studying the Casimir-Polder force [22,23].

II. EXPERIMENTAL RESULTS

Figure 2 shows a typical magnetic field scan above a room-temperature microwire array and the resulting image of the current density flowing through the wires. The FWHM point-spread resolution of the atomic density and magnetic field is $2.2(1)$ μm and can be improved in the future by more than a factor of 2 using a custom-tailored lens system. The current-density map has a lower spatial resolution than the field maps, stemming from the convolution of the field resolution with the typical distance $d = 1.4(1)$ μm between the atoms and sample. Distances as short as $0.8(1)$ μm shown in Fig. 1(c) may be used, providing a source resolution of $2.3(1)$ μm. Current flow through the microwires is clearly visible in Fig. 2(c), as is the fanning out of current into the bulk. Patches of lower current density may result from higher-resistance grains in the polycrystalline film, as measured in Ref. [8]. (See Appendixes A and B for resolution measurements, distance calibration, and scan done with the sample at cryogenic temperature.)

The accuracy, repeatability, linearity, and dynamic range of the magnetometer are shown in Fig. 3. The green line is a fit to the linear region of the measured versus applied current data and has a slope of 0.88(2). This slope implies an accuracy of 11(2)% and a responsivity only 11(2)% lower than that predicted for the high-sensitivity trap, $R = 1.97(3)$ nT/(atom/μm). The fields and current densities reported in Fig. 3 correspond to those calculated with a finite-element solver for the employed gold microwire dimensions to within approximately 10%.

The linear part of the dynamic range is between approximately ± 1.0 μA (± 40 nT). The upper limit arises due to the lack of atoms in the high-field regions, while the lower limit arises due to all the atoms pooling into the low-field regions, as may be seen in Fig. 3(b). The extended-dynamic-range trap provides a 3×-larger linear dynamic range, though with a responsivity 3× worse (see Appendix C). We employ a thermal gas to increase the dynamic range by approximately 50×, though at worse resolution and with approximately 100-fold-worse responsivity, as also noted in Refs. [7,8].

The repeatability, or average standard deviation in the data about the linear fit, is 2.3(3) nT per pixel, and the stability of the field measurement measured as the Allan deviation is 1.1(1) nT after 30 experimental runs. To calculate repeatability and Allan deviation, we extract the (shot-to-shot) deviations of the measured total current in the 12-μm wire by averaging the difference between the measured field profile and the predicted field profile (of the 12-μm wire); the repeatability and Allan deviation are spatial averages over the width of the calibration wire.

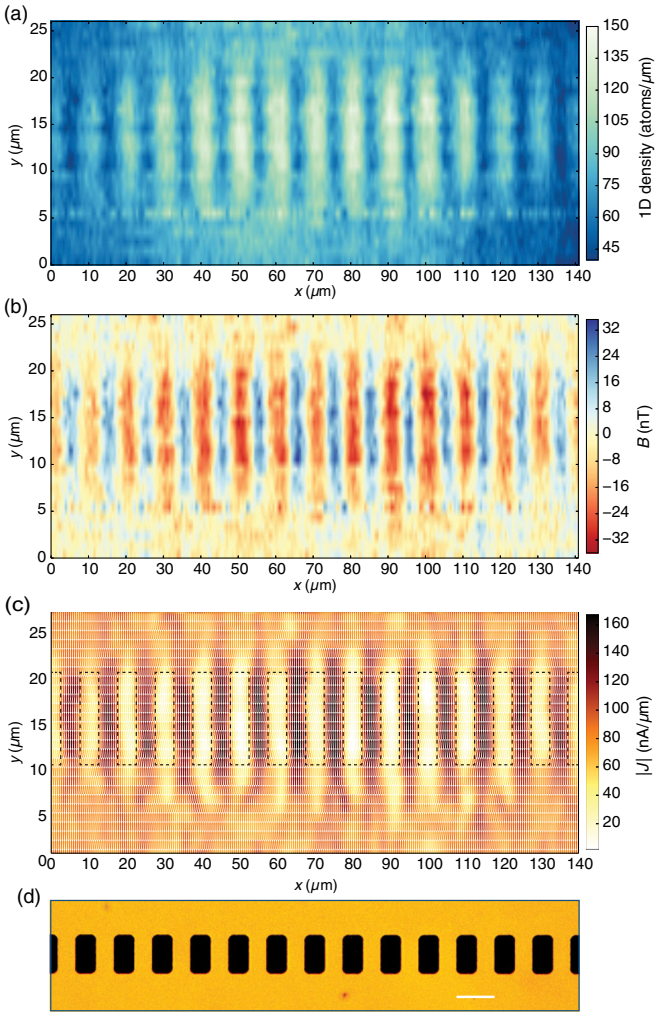

FIG. 2. Wide-area image of current density in the microwire array. Current flows through the room-temperature array of 5-μm-wide gold wires spaced 5 μm apart. Sample is scanned in 1-μm steps along $\hat{y}$. The BEC is confined $1.4(1)$ μm below using the extended-dynamic-range trap. (a) Line density of BEC. (b) Magnetic field along $\hat{x}$ derived from density data using the equation of state. (c) Current density obtained from magnetic field and measurement of d through the use of the Biot-Savart equation. Arrows indicate the current direction; the black dashed rectangles demarcate the gaps between the microwires. The current modulation away from the wires is likely due to inhomogeneously resistive grain boundaries, rather than noise, as explored in Ref. [8]. The spacing of arrows is given by our pixel size of approximately 0.54 μm, while our spatial resolution for current flow is $2.6(1)$ μm. (d) Image of the microwire array. White scale bar is 10 μm.

With no current applied to the sample, we measure a single-shot minimum sensitivity of 2.8(5) nT per pixel. (No spatial averaging is performed for this measurement.) This value is consistent with two independently measured quantum-noise-limited sources: photon shot noise accounts

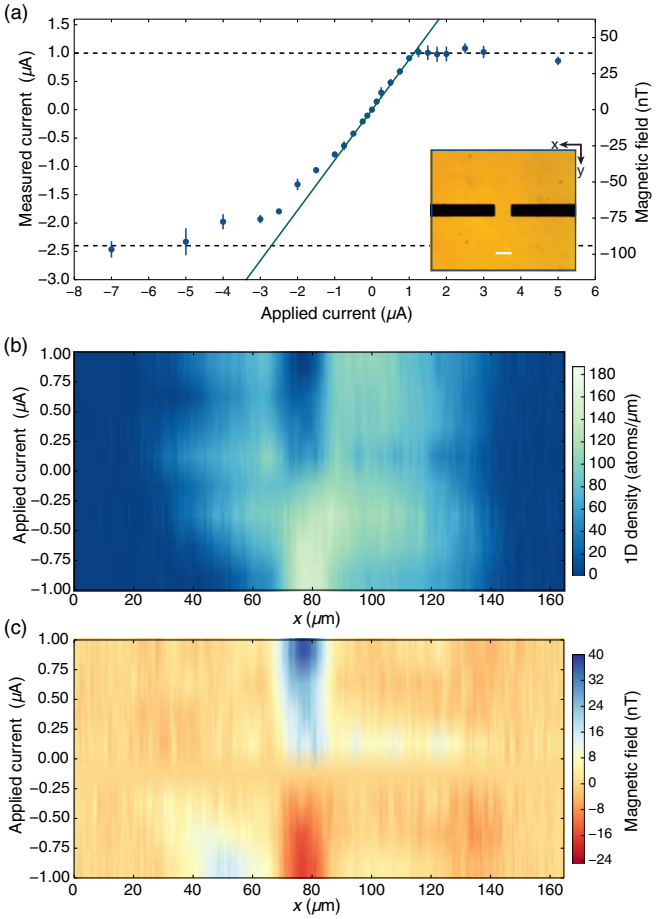

FIG. 3. SQCRAMscope accuracy, repeatability, linearity, and dynamic range. (a) Measurement of current in the 12-μm-wide calibration wire is shown in the inset. White scale bar is 12 μm. BEC is positioned 1.7(1) μm below the wire center using the high-sensitivity trap, and the current is varied to create either a density dimple or peak in the atomic density. The green line is a fit to the linear region. (b) Atomic line density versus applied current used for the data in panel (a). (c) Magnetic field in $\hat{x}$ calculated from data in panel (b).

for 2.5(4) nT per pixel, while atom density noise is 1.7(7) nT per pixel. Because of the quasicondensate nature of the gas, this noise is a factor of approximately 2 below that expected for shot noise in the higher-density regions of the BEC; hence, the use of "quantum" in the name of the scanning microscope. (See Appendix C for Allan deviation and noise measurements.)

The noise floor is measured also by Allan deviation, and the result is approximately 300 pT per pixel after 100 runs. (No spatial averaging is performed for this measurement.) This noise floor translates into a 2-nA minimum detectable current from an infinitely thin wire or 80 horizontally oriented $1\mu_B$ dipoles when the BEC is located $d = 0.8$ μm from these sources.

Since the particular pixel sizes are not intrinsic to the sensor itself, we now convert these "per-pixel" values to field sensitivities per our resolution-limited point (RLP)

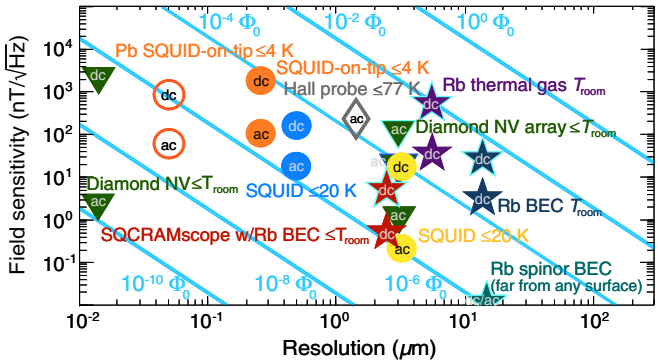

FIG. 4. Comparison to other scanning probes capable of imaging arbitrary field sources [1–3,6–8,24–30]. The diagonal cyan lines are contours of constant magnetic flux. Measurement bandwidth restrictions are labeled with "ac" or "dc". Temperature range capabilities are indicated. The star-shaped data markers are for BEC techniques. Points with a light blue outline denote single-point measurement sensitivity, while those without outlines (as well as the green triangle data marker with the blue outline) represent the sensitivity for parallel, multipoint measurements; see text. Addition of a heat shield to the SQCRAMscope—red stars—extends the temperature range from 35 K down to approximately 4 K.

size of 2.2 μm. The RLP is set by our spatial resolution for field measurements. There are 4.1(2) pixels per RLP for our lens system, and so the single-shot field sensitivity per RLP is a factor of $\sqrt{4.1}$ lower, or 1.4(1) nT. This is equivalent to 6.1(1) nT/$\sqrt{\text{Hz}}$ per RLP when considering the $\tau = 16$ s duty cycle.

The magnetometer simultaneously provides M-independent RLPs of information because the quasi-1D BEC may be several hundred microns in length while the imaging resolution is on the micron scale. This multipoint measurement provides an advantage over point-by-point scanning magnetometers such as SQUIDs because the SQCRAMscope can repeatedly measure these M points during the time MT it takes the scanning SQUID to sequentially measure the M points once. T is the integration time per point. That is, if $MT \gg \tau$, then the SQCRAMscope has enough time to average the signal of each RLP MT/τ times during the same time it takes the SQUID to record a single scan of the M points. This averaging process lowers the field sensitivity by a factor of $\sqrt{MT/\tau}$. In terms of sensitivity per root hertz, the enhancement factor is $\sqrt{M}$. This enhancement results in a field sensitivity of 590(80) pT/$\sqrt{\text{Hz}}$ per RLP for a line scan, given our $M = 200/2.2 = 91(5)$ and τ. Thus, high-sensitivity, high-resolution, and wide-area scans of condensed-matter samples can be made within a few hours. Future improvements can expedite this by reducing the duty cycle and elongating the usable BEC length. In Fig. 4, we include this parallel-measurement-based sensitivity in addition to the single-shot sensitivity to properly account for the parallel-scanning advantage of our sensor: that is, what

one cares about for comparing a parallel-scanning probe microscope is the sensitivity per point in the same time it takes a comparable point-by-point sensor to scan the same number of points.

III. COMPARISON TO OTHER TECHNIQUES

We now highlight other demonstrated features of the SQCRAMscope. Because the samples are physically detached from the chip, we can rapidly replace the sample without disturbing the BEC production apparatus in five days. This is much faster than the up to several months of current systems whose samples are attached directly to the atom chip. Second, the sample temperature may be independently controlled and stabilized, in contrast to samples attached to an atom chip, where trapping wire currents can uncontrollably heat the sample. In the case of superconducting atom-chip experiments such as in Refs. [31–39], the sample temperature is fixed to that of the superconducting chip and not tunable. The SQCRAMscope allows any approximately 1-cm^2 area, $\leq$150-μm-thin sample made of UHV-compatible material to be imaged from room temperature to cryogenic temperatures. We demonstrate here the functionality of the SQCRAMscope at room temperature and 35 K (see Appendix A) and believe operation down to approximately 4 K will soon be possible with the addition of a heat shield [10]. Lastly, we mention that because what the SQCRAMscope measures are nanotesla-strength, short-wavelength *deviations* in the mean field along the trap axis, the microscope is insensitive to much larger—up to hundreds of gauss—background or long-wavelength fluctuating fields along this axis. This feature obviates the need for careful magnetic field shielding of the apparatus.

In the following, we compare the scanning magnetometry capability of the SQCRAMscope to other high-source-resolution, high-sensitivity scanning probe magnetometers relying on field sensing of arbitrary sources rather than magnetic resonance of spins. (For the latter, see Refs. [28,40] for nanoscale diamond NV and magnetic-force-microscope-based techniques). See Fig. 4. Imaging the Larmor precession of spinor BECs has been used to measure magnetic fields with high sensitivity [29], though the technique has yet to be demonstrated near any surface, and so the technique's sensitivity limit near a sample is unclear.

By contrast, spin-polarized BECs have been used to image the field from and current flow through nearby room-temperature gold wires using the technique discussed here [5–8,41]. These works employed a BEC (thermal gas) $d = 10(3.5)$ μm from the room-temperature wires, resulting in a field sensitivity of approximately $4(42)$ nT/$\sqrt{\text{Hz}}$ per RLP at a current-density resolution of $11(5)$ μm to simultaneously measure 67(200) RLPs. We note that Refs. [6–8] do not include extensive calibration data, and so best-case estimates are used for comparison; i.e., we assume the reported resolution is FWHM rather than, e.g., 1σ, and that the reported *calculated* sensitivities are realized in their experiments (our calculated values are better than what we measure). As for our parallel sensor, the field sensitivity is obtained by multiplying their calculated minimum field by the square root of the ratio of duty cycle to the number of simultaneously measured RLPs (obtained from Refs. [42,43]). Again, the latter number is defined as the usable length of the cloud divided by the spatial resolution and is included because this instrument is intended as a scanning probe, and what matters is the entire time it takes to scan an area, not a point. To facilitate the comparisons to SQUIDs below, we estimate their magnetic flux sensitivity to be 10^{-4} $\Phi_0/\sqrt{\text{Hz}}$ by multiplying the minimum field sensitivity by the square of the current-density resolution.

By comparison, our present work lowers the minimum achieved field sensitivity to $0.6(1)$ nT/$\sqrt{\text{Hz}}$ per RLP for simultaneously measuring 91 points at a superior resolution of $2.3(1)$ μm (Rayleigh criterion). Moreover, we rigorously calibrate this field sensitivity from the use of a known test source in the form of gold microwires at both room and cryogenic temperatures. This results in nearly a 100-fold magnetic flux sensitivity improvement to 10^{-6} $\Phi_0/\sqrt{\text{Hz}}$. Lastly, unlike these previous experiments, our result derives from a true sample, one not part of the atom chip itself, and so it may be scanned for wide-area imaging, cryogenically cooled (to a temperature different than the chip temperature), and easily exchanged. All these features make our SQCRAMscope a versatile scanning probe atom microscope for condensed-matter materials.

The point-by-point scanning technique of SQUID magnetometers [2,3,24] provides high-ac-sensitivity $10^{-6}\Phi_0/\sqrt{\text{Hz}}$ (10–100× worse at dc) imaging at length scales from a few microns [24] to approximately 100 nm [2,3] and down to dilution refrigerator temperatures. [New SQUIDs-on-a-tip have achieved ac flux sensitivities of below 10^{-7} $\Phi_0/\sqrt{\text{Hz}}$ (dc, 10^{-6} $\Phi_0/\sqrt{\text{Hz}}$) [2], though with the use of fragile Pb-based superconductors.] The superior low-temperature and high-frequency imaging abilities of these scanning SQUIDs is complemented by the higher dc sensitivity and high-temperature compatibility of the SQCRAMscope. Specifically, these high-resolution SQUIDs lose sensitivity above sample temperatures of approximately 20 K due to weak thermal links to the sample, bringing the SQUID close to its superconducting critical temperature [25]. (High-T_c SQUIDs provide less sensitivity.) Moreover, SQUID sensitivity decreases by roughly 2 orders of magnitude at dc due to $1/f$ noise below approximately 100 Hz. We also note that while SQUIDs must often employ large fields to function, the SQCRAMscope is minimally invasive because the field at the trap bottom—and at the nearby sample—can be as small as 1 G. Conversely, however, our current SQCRAMscope is incompatible with the application of large fields perpendicular to the sample, though fields up to

nearly a kilogauss can be applied along the trap axis, in the plane of the sample.

Nanoscale scanning NV diamond magnetometers are also compatible with samples from room temperature to cryogenic temperatures [44] but are additionally operable outside ultrahigh vacuum. They provide a field sensitivity of a few $\mathrm{nT}/\sqrt{\mathrm{Hz}}$ with resolution down to a few nanometers near surfaces at frequencies above 10 kHz [1,27,28] and approximately 2 $\mu\mathrm{T}/\sqrt{\mathrm{Hz}}$ at dc with more than tenfold improvements predicted [45]. Arrays of NV sensors have been used for parallel, wide-area imaging of ac fields [26]. In Fig. 4, the three green triangle markers denote the sensitivity and resolution for these NV arrays for single-point measurements (light blue outline) at higher effective ac sensitivity (approximately 15 $\mathrm{nT}/\sqrt{\mathrm{Hz}}$ per RLP) with respect to the time it takes to integrate the same area as the raster line-scanned SQCRAMcope (shown with blue outline) and at still higher effective ac sensitivity (approximately 1 $\mathrm{nT}/\sqrt{\mathrm{Hz}}$ per RLP) with respect to point-by-point sensors (no outline). The SQCRAMscope complements this probe with its nearly 1000-fold higher dc sensitivity to fields that cannot be rapidly modulated. While the present approximately 2-μm-scale SQCRAMscope resolution is far worse than single-NV probes, a SQCRAMscope with submicron resolution is possible as well as with ac sensitivity at bandwidths up to approximately 10 kHz via dispersive imaging [29] and up to approximately megahertz using Rabi spectroscopy [46].

IV. OUTLOOK

The low dc-field sensitivity and wide temperature compatibility of the SQCRAMscope provides the ability to investigate phenomena in materials outside the reach of the current capabilities of, e.g., scanning SQUIDs. We highlight here one such application for which the SQCRAMscope is suited. The possible emergence of the unconventional pair-density-wave superfluid state in cuprate, high-T_c superconductors and the theory of striped superconductors is the subject of much interest and speculation [47,48]. A key signature of such a state is the spontaneous generation of dc currents around domains of the emerging chiral superconductor as the temperature is tuned below the transition at approximately 30 K. Imaging transport may reveal these spontaneously generated current loops. However, while the length scale of current loops may be on the few-micron scale and, thus, within our detection range, it is not theoretically known what might be the magnitude of the currents and detection has been elusive [49]. Thus, one requires a sensor of highest dc sensitivity to maximize one's chances of observation and to bound this magnitude if no signal is observed. The SQCRAMscope is positioned to tackle this important measurement: its dc sensitivity is 2 to 3 orders of magnitude greater than SQUIDs and NV diamonds, and scanning a wide field of view is necessary to hunt for the chiral currents as they emerge, a task appropriate for the SQCRAMscope with its parallel-sensing capability. Moreover, the high ac sensitivity of those sensors is not relevant since the spontaneously generated currents cannot be modulated, and SQUIDs become less sensitive at the elevated temperature at which the transition is predicted to occur. In summary, the SQCRAMscope enables the study of strongly correlated and topologically nontrivial materials in relatively unexplored regimes of parameter space.

ACKNOWLEDGMENTS

We thank M. Naides, J. DiSciacca, S. Qiao, and J. Straquadine for experimental assistance, and P. Abbamonte, J. Analytis, S. L. Cooper, I. Fisher, J. Kirtley, S. Kivelson, M. Lukin, K. Moler, R. Walsworth, and A. Yacoby for stimulating discussions. This work is supported by the U.S. Department of Energy, Office of Science, Basic Energy Sciences under Award No. DE-SC0012338 (equipment and materials, and support for B. L. L.). R. W. T., A. J. K., and B. L. L. acknowledge support from the Gordon and Betty Moore Foundation through Grant No. GBMF3502.

APPENDIX A: EXPERIMENTAL METHODS

1. Cryogenic scan

The cryogenic capability of the trapping apparatus is demonstrated in Ref. [10]. While the majority of the data shown here were taken at room temperature, we perform a magnetometry scan shown in Fig. 5 at 35 K with no discernible loss in capability, other than the observation of a horizontal drift in the relative BEC-sample position. This drift is likely due to the slow settling of thermally contracting parts of the apparatus and can be mitigated by waiting longer before imaging. The temperature is measured with in-vacuum thermometers contacted to the cold head and calibrated to the temperature at the sample tip [10].

2. Calibration sample

The sample substrate is a 150-μm-thick wafer of oxidized intrinsic $\langle 100 \rangle$ silicon. The gold calibration wires are fabricated directly onto the sample substrate using photolithography, as shown in Fig. 6(a), and positioned using a three-axis translation stage, such that the calibration wires are approximately 300 μm below the atom chip. See Ref. [10] for more details. We verify that the quasi-1D BEC located below the calibration wires is not fragmented by meandering currents in the atom chip's microwires at this far distance. The stage can move the sample substrate 3.8 mm in $\hat{x}$ and 5.4 mm in $\hat{y}$ allowing any sample feature within this area to be placed in proximity to the BEC. (Future improvements will increase this area by approximately 5×.) The coarse positioning of the BEC with respect to the microwire arrays on the calibration sample is made by fluorescence imaging from below the sample.

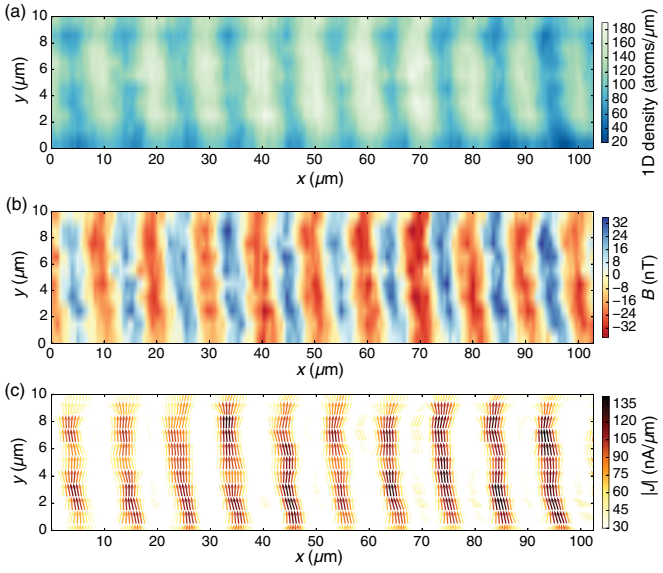

FIG. 5. Scan under cryogenic conditions. Sample at 35 K. Scan over the central region of the same microwire array as in Fig. 2. The wires are 5 μm wide and spaced 5 μm apart. The sample moves in 1-μm steps along $\hat{y}$. The BEC is confined 1.2(1) μm below it using the extended-dynamic-range trap. (a) Line density of atoms. (b) Magnetic field along $\hat{x}$. (c) Current density. Arrows show the direction of current flow. The spacing of arrows is given by our pixel size of approximately 0.54 μm, while our spatial resolution for current flow is 2.5(1) μm.

Fine positioning is performed by fitting magnetic field profiles obtained from magnetometry of current flowing through sample calibration features. Microwire centers are found to within 1 μm.

Vertical vibrations of the cantilevered calibration sample at frequencies larger than approximately 1 Hz are 150-nm rms, much less than our imaging resolution, and may be ignored [10]. Thermal expansion of the atom chip and the sample mount assemblies cause small drifts of the sample position relative to the BEC on a time scale much slower than the duty cycle. However, these are easily measured via imaging and canceled via feedforward to the bias field that controls the atom-chip trap height between each run. More difficult to cancel are vertical drifts at the time scale of the duty cycle. These cause approximately 0.5-μm shot-to-shot fluctuations of the BEC position d relative to the sample. Fortunately, these may be accounted for in the data analysis on a shot-to-shot basis since d is imagined at the same time as the atomic density. The BEC scan data and accuracy calibrations reveal that the horizontal movements of the sample stage with respect to the imaging system are less than 0.5 μm shot to shot at room temperature.

The data for Figs. 1–3 are taken using the sample shown in Fig. 6(b). We use e-beam evaporation, photolithography, and ion milling to fabricate the 400-nm-thick gold calibration wire patterns. The calibration sample contains two 1.2-mm-wide strips of gold, as sketched in Fig. 6(c). Gaps in the gold of these strips define microwires and microwire arrays of different sizes and spacings, as shown in Fig. 6(d)–6(f). Current flowing through the constricted regions provides the signal for all measurements. The microwire arrays in Figs. 6(e) and 6(f) are periodic with equal wire width and spacing. The magnification calibration in Fig. 7 and resolution calibration in Figs. 12(b)–12(d) are taken with a different calibration sample (not shown),

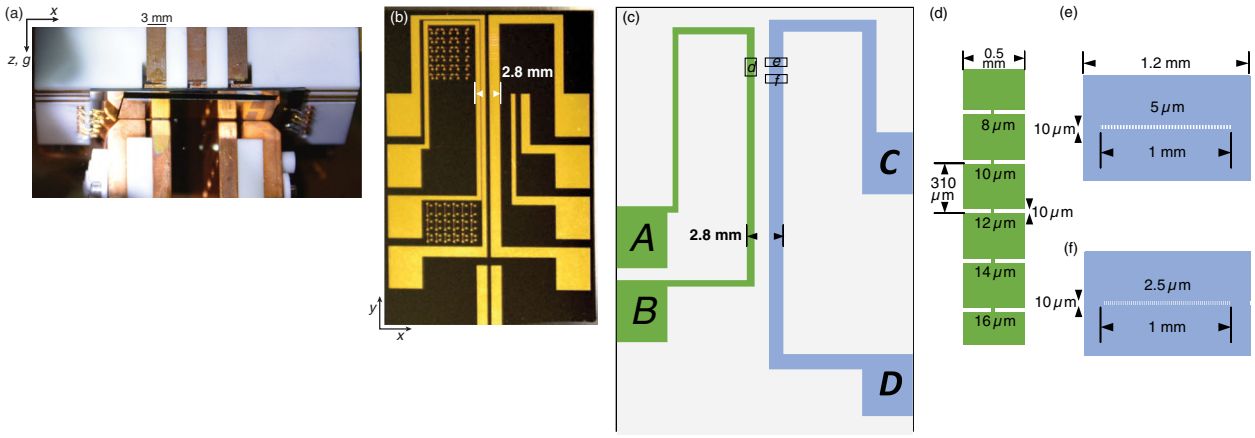

FIG. 6. Calibration sample schematic. (a) Image of gold-coated silicon sample substrate 200 μm below the atom chip. The copper leads for the macrowire trap may be seen above the atom chip, and the trench through which the imaging beam passes is visible below the center of the sample substrate. (b) Picture of the calibration sample. (c) Schematic of the subset of wires in the calibration sample used for this work. The green wire between contacts A and B supports the single-microwire features shown in the close-up in (d), while the blue wire between contacts C and D supports the arrays of microwires, two of which are shown in (e) and (f). The letters surrounded by black boxes denote the wire regions sketched in panels (d)–(f). (d) Schematic of the single-microwire features, with the 12-μm-wide feature used for the data in Figs. 3, 14, and 17. (e) Schematic of periodic array of 5-μm-wide microwires spaced 5 μm from one another. This feature is used for the wide-area scans in Figs. 2 and 5. (f) Schematic of periodic array of 2.5-μm-wide microwires spaced 2.5 μm from one another. This feature is used for the image in Fig. 1(c) and the resolution data in Fig. 13.

which contains an array of microwires of width 2.0(1) μm and length 10 μm spaced 20.0(2) μm from each other.

3. Quasi-1D BEC production

Atom-chip trapping of ultracold gases of ^{87}Rb atoms proceeds in a manner similar to that described in Ref. [10]. Briefly, 4×10^7 atoms in the $|F, m_F\rangle = |2, 2\rangle$ ground state at 30 μK are loaded into an optical dipole trap (ODT). (The g factor is $1/2$ in this weak-field-seeking state.) These atoms are then transported 33 cm by moving the lens focusing the ODT. The atoms pass through a gate valve into a science chamber. The gate valve allows samples within the science chamber to be exchanged without breaking the ultrahigh vacuum of the production chamber. The room-temperature vacuum of the science chamber is below 6.5×10^{-11} Torr, sufficient for BEC production using the atom chip; see Refs. [9,35] for details on BEC production using atom chips. This pressure decreases upon the cryogenic cooling of the sample [10].

The ODT is located 3.5 mm below the atom chip so as not to heat the sample and chip with scattered light. To bring the atoms closer to the sample, the atoms are transferred from the ODT to a magnetostatic harmonic trap formed by an H-shaped Cu wire and a homogeneous field. The wire is mounted just above the atom chip, which faces downwards. See Fig. 6(a) and Ref. [10]. This macrowire magnetic trap is moved upwards to within a few hundred microns of the chip. Atoms are then transferred to an atom-chip-based trap. The trap in the $\hat{y}$-$\hat{z}$ plane is formed with three wires: a bias magnetic field along $\hat{y}$ is created by macrowires on either side of a 150-μm-wide wire whose current flows opposite to the macrowires; all currents in these wires can be rapidly shut off to drop the atoms for short time-of-flight (TOF) imaging. Weak confinement along the axis of the quasi-1D BEC is provided by independently controlled orthogonal end-cap wires. rf evaporation produces BECs with up to a few 10^4 atoms. The entire procedure is typically repeated every 20 s, though 16-s cycle times can be used.

We create BECs in two different traps. The first, the high-sensitivity trap, is optimized to minimize single-shot repeatability and detectable field. (Lower transverse trap frequency leads to higher sensitivity through the minimization of mean-field energy but also reduces the dynamic range due to lower density.) The trap frequencies are $\omega_\perp = 2\pi \times 710(10)$ Hz and $\omega_x = 2\pi \times 4.48(3)$ Hz, and we create quasi-1D BECs of $7.0(4) \times 10^3$ atoms at temperature 12(1) nK. (Larger BECs are possible, but the lower population ensures operation within the quasicondensate regime.) This temperature is far below the quasidegeneracy temperature 1.5(1) μK—the critical temperature for phase fluctuations is 9.0(5) nK—and 2.8× below the temperature associated with $\omega_\perp$, 33.7(6) nK [11–13]. (See Appendix C for a discussion of the temperature measurement.) The chemical potential is 32(1) nK, similar to $\omega_\perp$ and sufficiently low for the quasicondensate equation of state to hold to high accuracy [11]. Shot-to-shot temperature and number fluctuations do not affect the magnetometry because they are not sufficiently large to change the applicable equation of state for the gas and are recorded and accounted for on a shot-by-shot basis. The second trap, with frequencies $\omega_\perp = 2\pi \times 1810(30)$ Hz and $\omega_x = 2\pi \times 4.1(1)$ Hz, is optimized to extend the dynamic range while also providing 1D Bose gases within the quasicondensate regime.

After quasicondensate preparation, the current in the calibration wire is adiabatically ramped up in 300 ms. The BEC is then raised to a distance 1.7(2) μm below the sample surface for the high-sensitivity trap and 1.3(4) μm below the sample for the extended-dynamic-range trap. The lifetime within the trap is greater than 700 ms at $d > 1$ μm; the attractive Casimir-Polder potential does not pose a severe lifetime limit at this distance [22].

APPENDIX B: IMAGING CALIBRATION

1. Imaging

BECs are held in the magnetic field of the calibration sample for approximately 250 ms before the trap and sample fields are rapidly removed for BEC imaging. This is much longer than the density response time of approximately 0.5 ms, the time atoms take to move approximately 1 μm at the speed of sound in the BEC [50]. We allow the atoms to fall for 150 μs. The imaging beam is on for 20 μs, during which the atoms diffuse by approximately 500-nm rms, much less than our imaging resolution (see below). During this brief TOF, the atoms fall approximately 1 μm due to gravity and an initial velocity imparted from magnetic gradients when the trapping fields are turned off. The imaging takes place when the atoms are approximately 2.5 μm from the sample (see below). Ballistic expansion during this time is approximately 200 nm and also small compared to the imaging resolution.

An accurate measurement of the imaging magnification via the rate of fall under gravity is problematic due to the small field of view in the vertical direction. This is the result of our high magnification and the use of only a small fraction of our CCD array so that the fast kinetics mode can be used for fringe suppression. We, therefore, measure the magnification by imprinting a density modulation of known periodicity onto the gas and imaging its density *in situ* with no TOF. See Fig. 7. The density modulation is created by using the magnetic fields from a microfabricated microwire array on a calibration sample. The error in the spatial frequency measurement combined with uncertainty in the microwire dimensions leads to a 0.8% uncertainty in magnification.

Imaging the BEC near a surface is complicated by the presence of diffraction fringes from the sample edge. Reflecting the absorption imaging beam at a small angle θ removes the fringes from the field of interest [51], but it

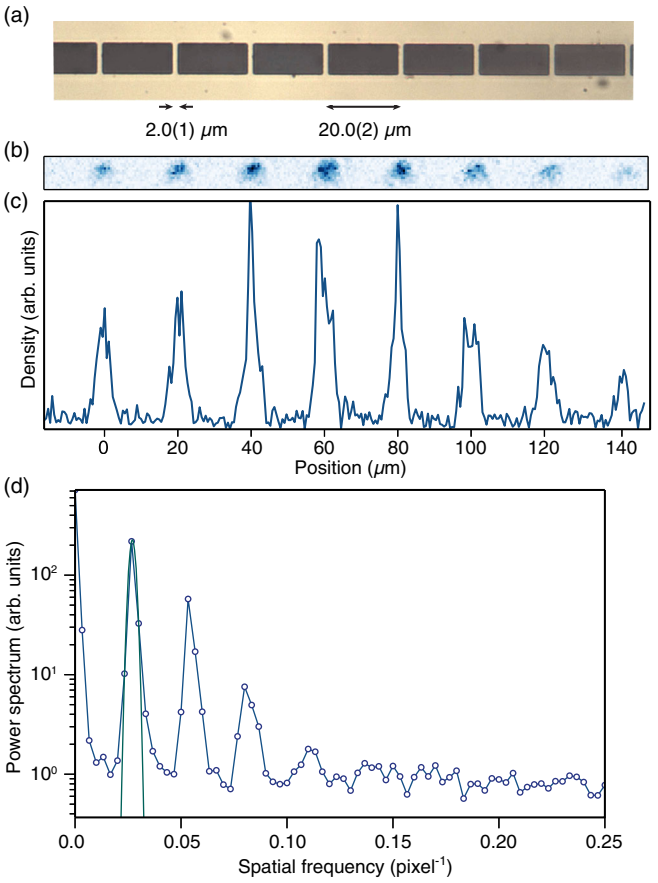

FIG. 7. Magnification calibration. (a) Image of the calibration wire array with 2.0(1) μm-wide wires spaced 20.0(2) μm apart. (b) Absorption image of BEC fragmentation and (c) density of atoms versus position. (d) Power spectrum versus spatial frequency. Green curve is the fit to the fundamental harmonic from which we determine a magnification of 24.0(2). This is consistent with the geometrically determined value of approximately 24. Blue lines connecting the data points are guides to the eye.

introduces a standing-wave intensity pattern perpendicular to the chip. (Nonreflective samples may be coated with a thin insulator before mirroring with gold; a gold mirror and insulating layer need be only a few hundred nanometers, far thinner than our optical resolution.) This nonuniform intensity pattern complicates the usually simple technique of absorption imaging commonly employed in free space, away from reflective surfaces. Moreover, due to the reflection, the polarization of the imaging beam must be linear and parallel to the sample surface to prevent polarization imperfections at the position of the atoms. To define the quantization axis during imaging, we maintain a small B field along this polarization direction. The light drives π transitions, resulting in non-closed-cycle transitions. However, we use numerical simulations of the optical Bloch equations to account for the optical pumping out of the trapped $m_F = 2$ state during the imaging time; we use in our calculations the effective cross section σ_0 obtained from these simulations. (This also accounts for the α^* term in Ref. [52].) We now describe how to perform absorption imaging in the presence of the standing wave pattern. Figure 8 depicts the imaging geometry.

The main points that must be considered are (1) the atoms appear in two images on the CCD, a mirror image from field $\vec{E}_1$ and a real image from the reflected field $\vec{E}_2$, as shown in Fig. 8. By mirror image, we mean that the light scatters first from the atoms before reflecting off the mirror into the imaging system. We use the average of the mirror image and the real image for the data in this work. (2) The mirror is finite in extent and, therefore, acts as a Fourier filter for shallow-angle components that are not reflected into the imaging system [51]. That is, the upward scattering fields from E_1 and E_2 are not imaged onto the CCD since their negative k_z components do not get reflected from the mirrored sample. While this can lead to image distortion, it is a negligible perturbation for mirrors as long and d's as small as ours. (3) Angular aliasing: for narrow gases of atoms imaged at small θ, light scattered away from the mirror at angles larger than θ are represented in the imaging system as having come from the actual gas location (see Ref. [51]). This effect blurs the lower half of the gas image in $\hat{z}$, and the atom number can be miscounted for a gas much narrower than an imaging resolution such as ours. However, this aliasing is not an issue for our system because of the high-saturation imaging we employ; summing over the apparent density in $\hat{z}$ counts all the atoms due to the linearity of the solution to Beer's law in this limit (see below). (4) The standing-wave intensity pattern changes the local rate of scattering. For example, atoms located at the node of the standing wave do not register on the camera. (5) The interference pattern is not present at the CCD plane because $\vec{E}_1$ and $\vec{E}_2$ from the imaging beam are recorded on separate areas of the CCD. As a consequence, there are

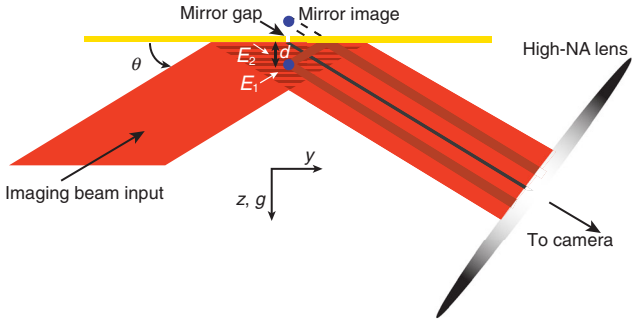

FIG. 8. Geometry of the absorption imaging beam reflecting off the gold mirror of the calibration sample. (Not to scale.) Gaps in the gold mirror, which define the microwires, also cast shadows onto the reflected beam. By design, however, the height of the shadow at the position of the BEC is much less than d. Nonreflective samples may be coated with a thin insulator before mirroring with gold; a gold mirror and insulating layer need be only a few hundred nanometers, far thinner than our optical resolution.

field components recorded by the CCD camera that are not present at the atoms.

The effects of points (4) and (5) are non-negligible and must be taken into account to obtain an accurate measurement of atom density. We do so by modifying Beer's law for the case of absorption imaging an optically dense gas near a reflective surface with high optical resolution. We present a thorough discussion of this derivation because it is crucial to the high accuracy achieved by the SQCRAMscope.

In order to measure the atomic density, we take three images 1.5 ms apart. In the first image, the atoms are illuminated by the probe beam, and this casts a shadow on the imaging system with intensity profile P^F. The second image is taken without the atoms present, yielding P^I at the imaging system. Finally, a third background image is taken in the absence of both the probe beam and the atoms to measure any stray light incident on the camera. This background image is then subtracted from the first two images.

Traditional absorption imaging is performed well below the atomic saturation intensity I_{sat} so that power scattered by the atoms is proportional to the probe intensity. In this regime, the atomic scattering rate is given by $\rho\sigma_0 I$, where σ_0 is the effective atomic cross section, and $\rho(x,y,z)$ is the volume density of the cloud. This leads to Beer's law, a differential equation $dI/dy = -\rho\sigma_0 I$ that describes the evolution of the probe beam intensity. It supports an exponentially decaying solution resulting in $n\sigma_0 = -\ln(I^F/I^I) = -\ln(P^F/P^I)$, where $n(x,z)$ is the atomic column density, $I^I(x,z)$ is the incoming intensity, and $I^F(x,z)$ is the intensity after passing through the gas. For free-space imaging, the measured intensities are directly related to the intensities at the atomic position: $P^I = I^I$ and $P^F = I^F$.

This simple, low-intensity imaging method found sufficient for other atom-chip systems [51] cannot be used in our high-magnification, high-optical-depth system: the large magnification of our high-resolution imaging system means that low probe intensities correspond to very low count levels on the camera, while the high optical density (OD) of our nearly *in situ* BEC means that almost all of these few photons are absorbed. The atomic response is saturated, resulting in low dynamic range. Detuning off resonance reduces the OD but at the expense of image distortions due to the dispersive atomic medium. We, therefore, choose to operate in the opposite regime of large probe intensity to completely saturate the atomic response [52]. In this regime, a new term must be included in the equation for n. In the case of resonant imaging with a single traveling-wave beam in free space, the relation becomes

$$n\sigma_0 = -\ln(I^F/I^I) + (I^I - I^F)/I_{\text{sat}}. \tag{B1}$$

For the probe intensities used here, the second linear term is the dominant contribution, rather than the first nonlinear term, as in low-intensity imaging. This is advantageous for systems such as ours in which large variations in the column density can occur on length scales smaller than the imaging resolution. Specifically, such effects cause P^F to differ from I^F, with the result that Eq. (B1) does not yield the actual *in situ* density. The discrepancy can be large in the $\hat{z}$ direction transverse to the BEC axis where the gas is smaller than the imaging resolution. But since the measured magnetic field depends only on $n_{1\text{D}}(x)$, the integral along z of the column density $n(x,z)$, it is sufficient to determine the total column density integrated along the $\hat{z}$ direction. That this integral accurately counts the atoms is due to the linearity of Eq. (B1) in the high-intensity imaging limit.

The intensity pattern at the atoms consists of two interfering traveling waves: $\vec{E}_1(x,y,z)$ due to the portion of the imaging beam that passes through the atoms before reflecting off the sample and $\vec{E}_2(x,y,z)$ due to the portion that reflects before passing through the atoms (see Fig. 8). Restricting our attention to the region of the interference pattern near the atoms and assuming equal intensities in both beams, the magnitudes are related by $|E_2(y,z)| = |E_1(y,z)| \equiv \mathcal{E}(y,z)$ in the limits that the angle of incidence to the sample is small and that the gas size is small compared to the wavelength of the standing wave. These conditions are well satisfied in our system. Specifically, the two fields take the form

$$E_1(y,z) = \mathcal{E}(y,z)\exp(ik_\parallel y + ik_\perp z), \tag{B2}$$

$$E_2(y,z) = -\mathcal{E}(y,z)\exp(ik_\parallel y - ik_\perp z), \tag{B3}$$

where $k_\parallel$ is the projection of the wave vector onto the y direction parallel to the sample, $k_\perp$ is the projection of the wave vector onto the z direction perpendicular to the sample, and the minus sign accounts for the phase shift imparted by reflection off the sample. The total electric field takes the form

$$E(y,z) = 2i\mathcal{E}(y,z)\sin(k_\perp z)\exp(ik_\parallel y), \tag{B4}$$

which gives rise to the interference pattern in the intensity at the atoms of

$$I(y,z) = 4\mathcal{E}^2(y,z)\sin^2(k_\perp z). \tag{B5}$$

To calculate the measured P intensities from the I's, we now must relate $|E_1|^2$, which is the field that forms the upper mirror image on the camera, to I, which sets the atomic scattering rate. One must contend with the fact that the two fields E_1 and E_2 propagate in different directions and so are imaged without interference at separate locations on the CCD. The analog of Beer's law is, therefore, two coupled differential equations whose solutions describe the evolution of the field E_1 from E_1^I to E_1^F and E_2 from E_2^I

to E_2^F. These equations are coupled by an atomic scattering term, though a change in notation decouples them. Dropping the coordinate arguments for notational ease, we write for the initial fields

$$E_1^I = E_{a1}^I + E_{b1}^I, \tag{B6}$$

$$E_2^I = E_{a2}^I + E_{b2}^I, \tag{B7}$$

where

$$E_{a1}^I = E_{a2}^I = i\mathcal{E}^I \exp(ik_\parallel y)\sin(k_\perp z), \tag{B8}$$

$$E_{b1}^I = -E_{b2}^I = \mathcal{E}^I \exp(ik_\parallel y)\cos(k_\perp z). \tag{B9}$$

By contrast,

$$E_{a1}^F = E_{a2}^F = i\mathcal{E}^F \exp(ik_\parallel y)\sin(k_\perp z), \tag{B10}$$

$$E_{b1}^F = -E_{b2}^F = \mathcal{E}^I \exp(ik_\parallel y)\cos(k_\perp z). \tag{B11}$$

Note that the E_b^F's are proportional to $\mathcal{E}^I$ since they are not attenuated by the atoms. This is because the E_b^I field components cancel in the interference region. The intensity of the standing wave before the atoms is simply

$$I^I = |E_{a1}^I + E_{a2}^I|^2 = |2E_{a1}^I|^2 = 4|\mathcal{E}^I|^2 \sin^2(k_\perp z), \tag{B12}$$

while after the atoms it is

$$I^F = |E_{a1}^F + E_{a2}^F|^2 = 4|\mathcal{E}^F|^2 \sin^2(k_\perp z). \tag{B13}$$

We now relate the intensities immediately before and after the atomic position to the intensities $P_{1,2}^I$ (without atoms) and $P_{1,2}^F$ (with atoms) at the imaging system where the fields $\vec{E}_1$ and $\vec{E}_2$ no longer overlap. We now focus our attention on the mirror image, and the case for the real image is analogous. Because E_{a1}^I and E_{b1}^I are $\pi/2$ out of phase,

$$P_1^I = |E_{a1}^I|^2 + |E_{b1}^I|^2 = |\mathcal{E}^I|^2, \tag{B14}$$

while

$$P_1^F = |E_{a1}^F|^2 + |E_{b1}^F|^2 = |\mathcal{E}^F|^2 \sin^2(k_\perp z) + |\mathcal{E}^I|^2 \cos^2(k_\perp z). \tag{B15}$$

By eliminating $\mathcal{E}_I$ and $\mathcal{E}_F$, we arrive at the relations

$$I_1^I = 4P_1^I \sin^2(k_\perp z), \tag{B16}$$

$$I_1^F = 4P_1^F - 4P_1^I \sin^2(k_\perp z), \tag{B17}$$

and the solution to the modified Beer's law in terms of the measured intensities becomes

$$n\sigma_0 = -\ln\left[\frac{P_1^F}{P_1^I} + \left(\frac{\sin^2(k_\perp z) - 1}{\sin^2(k_\perp z)}\right)\frac{P_1^I - P_1^F}{P_1^I}\right] + 4\frac{P_1^I - P_1^F}{I_{\rm sat}} \approx 4\frac{P_1^I - P_1^F}{I_{\rm sat}}. \tag{B18}$$

The last relation is valid under the assumption that we are operating in the high-intensity regime defined by $\min(I^F) \gg I_{\rm sat}$. As we discuss above, this provides larger dynamic range in the photon detection, while also providing the ability to accurately determine atom density in the presence of a finite imaging resolution due to the linearity of this expression. Whether this criterion applies depends on the distance of the BEC from the sample since atomic clouds near the nodes of the standing wave experience lower incident probe intensities. That this criterion is satisfied is ensured by our short TOF which places the BEC close enough to the first antinode of the standing wave below the mirrored sample for $\min(I^F) \gg I_{\rm sat}$, while also providing a nearly *in situ* measurement of the atomic density. Satisfying the criterion also depends on the peak column density, because for high-OD gases, it is possible for $I^F < I_{\rm sat}$ even if $I^I \gg I_{\rm sat}$. While our quasi-1D BEC has a high OD at short TOF, care is taken to employ sufficiently high probe intensity to satisfy the high-intensity criterion for all ODs encountered.

2. Distance from the sample

All distance measurements rely on knowing the angle θ that the imaging beam makes with the sample. The periodicity of the interference pattern is measured by scattering the reflected beam off a large gas of thermal atoms located within the interference region. The resulting periodic modulation of the absorption of the atoms reveals the intensity modulation of the inference fringes. See Fig. 9. A sinusoidal fit provides the periodicity of these fringes λ', which is related to the angle of incidence θ through $\theta = \arcsin(\lambda/\lambda')$, where λ is the ^{87}Rb D_2-transition wavelength. The angle for our measurements is $\theta = 2.26(2)°$.

At this shallow angle of incidence, the distance d of the gas from the sample surface is half the distance between the mirror and real images of the atoms. See Figs. 8 and 10. Below $d \lesssim \sigma_\perp$, the two images merge, where $\sigma_\perp$ is the apparent transverse width of the gas (either physical or imaging resolution limited). The height can be determined by fitting the images to two Gaussians of fixed width (known from images with $d > \sigma_\perp$) and choosing the center separation which best reproduces the observed total width. This results in a tenfold increase in height uncertainty to 13% when imaging gases below $d \approx 1$ μm.

Our data are taken at a short TOF such that the distance d' to the sample at the time of imaging is closer to the first antinode of the imaging light standing wave and is in the $d' > \sigma_\perp$ regime of two discernible Gaussians. Fits to the resulting images provide an uncertainty on d' of 60 nm. To

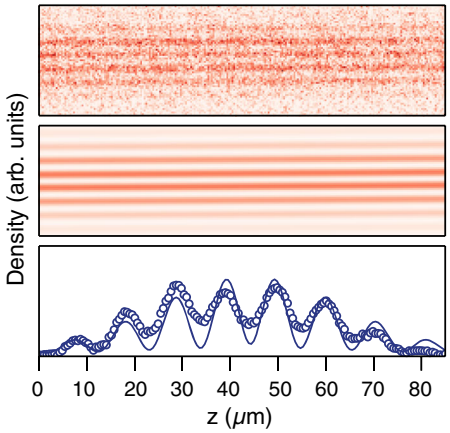

FIG. 9. Reflection angle measurement. Top: Absorption image of a thermal gas in the beam's interference pattern. Middle: Simulation of the interference pattern. Bottom: The imaging beam angle θ is measured via a fit of the simulation's fringe periodicity to the data.

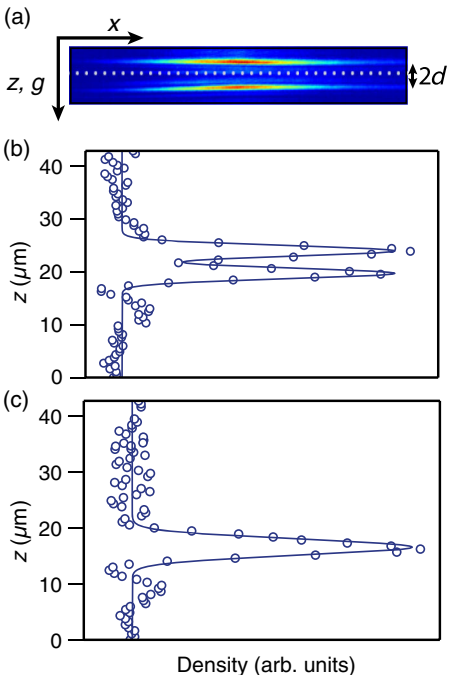

FIG. 10. Calibration of distance below the sample. (a) Example of *in situ* absorption image showing the real (lower) and mirror (upper) images equidistant from the mirrored sample surface (demarcated by white dots). (b) Example of a measurement of the distance of the atoms from the surface d. The density is integrated along $\hat{x}$ of an image such as that shown in panel (a). The width and positions of the double Gaussian profiles are left as free variables, resulting in $d = 4.24(6)$ μm. (c) Fit to BEC close to the sample, using fixed BEC width, resulting in $d = 0.8(1)$ μm.

find the uncertainty of d, we combine in quadrature this fit uncertainty with the uncertainty of inferring the height difference δd between the *in situ* d and d'. We determine this error using two methods: the first from repeated sequential measurements of the atoms at d and d' and the second from the time needed for free fall with an initial velocity imparted onto the atoms from the magnetic field gradients produced during trap release. The first method yields an error on δd of 50 nm (60 nm) for the high-sensitivity (extended-dynamic-range) trap. For the second method, we need to measure the time of free fall t and the initial velocity v. The time between trap release and imaging is $t = 148(5)$ μs, which has contributions from the time needed to turn off the wire currents, the programmed TOF time, and the imaging duration. The velocity is measured by a series images of the atoms just after release and yields a $v = 5.5(3)$ $[9.9(2)]$ μm/ms for the high-sensitivity (extended-dynamic-range) trap. Together, these result in errors on δd of 60 nm for both traps, roughly consistent with the first method. We assign an error of 60 nm to both traps' δd, resulting in a total error on d of 80 nm.

The microwires used to perform all measurements are 10 μm in length, with gaps in the gold-coated surface on either side. These gaps in the mirror surface result in shadows in the interference pattern above the sample. However, this region extends only 180 nm below the region of the microwires, and, therefore, the shadow is not cast onto the gas trapped approximately 1 μm below. See Fig. 8. The microwire arrays are spaced 300 μm apart so that the shadow from neighboring microwire arrays passes well below the BEC.

3. Resolution

The first lens of the imaging system is an off-the-shelf 31.25-mm focal length aspheric lens. This is followed by a 24× telescope chosen such that each pixel of the CCD camera is 542(5) nm wide in the object plane and well below our imaging resolution. Future work will employ a custom lens system for improved resolution.

The resolution of the current imaging system is measured in four ways. First, we image the 1951 Air Force Test Target out of vacuum but through an identical bucket window to the one used for the science chamber. The window is tilted at approximately 2.5° to approximate the angle of the absorption beam reflected off the mirrored sample. Figure 11 shows a measurement of contrast versus line pairs per millimeter, from which we determine a minimum observable line width of $2 \times 1.11(5)$ μm and a line pair resolution of $2.2(1)$ μm. This resolution is approximately 20% larger than the geometrically determined 1.8-μm diffraction limit (Rayleigh criterion) of the lens system.

We perform three *in vacuo* measurements. The first shown in Fig. 12(b) is a measurement of the transverse width in $\hat{z}$ of the quasi-1D BEC. The 1σ width is $0.8(1)$ μm, indicating a FWHM resolution of $1.9(1)$ μm. Assuming a cylindrically symmetric trap, the resolution in $\hat{y}$ is at least approximately $1.9(1)$ μm for single-shot measurements, but from our knowledge of trap parameters

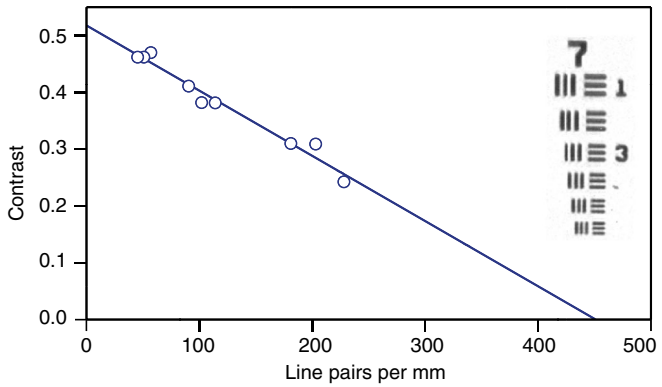

FIG. 11. Resolution measurement with the test target. Resolution measured through a viewport not under vacuum using the 1951 Air Force Test Target, the image of which is shown in the inset. The zero-contrast x intercept indicates a resolution of $2.2(1)$ μm.

and density, we believe the $\hat{y}$ resolution is closer to the FWHM width of the BEC, 950 nm, convolved with d. (The stepping resolution the translation stage is 10 nm.)

The next two methods measure the *in situ* resolution in $\hat{x}$. First, we utilize a dimple trap formed by running current in the 2-μm-wide microwire array shown in Fig. 12(a). The BEC above these sparsely spaced wires fragments into a chain of dots, the width of one of which, shown in Fig. 12(c), we measure as a function of the atom number. Figure 12(d) shows the 1σ radius of the dot of Bose condensed atoms as repulsive mean field energy is reduced by trapping fewer atoms in the initial condensate. The trap population is controlled by changing the rf evaporation cooling time. Extrapolating to zero atoms, we obtain a Gaussian point-spread function width of $2\sigma = 2.2(2)$ μm, for a FWHM resolution of $2.6(2)$ μm.

The last method shown in Fig. 13 uses an array of 2.5-μm-wide wires spaced 2.5 μm apart and finds the mean 1σ width of the dots of atoms in each of the microtraps. The mean 1σ width is $1.0(1)$ μm, implying a FWHM resolution of $2.4(2)$ μm. All of these methods are consistent with one another within less than 2σ. We choose to take the adjusted

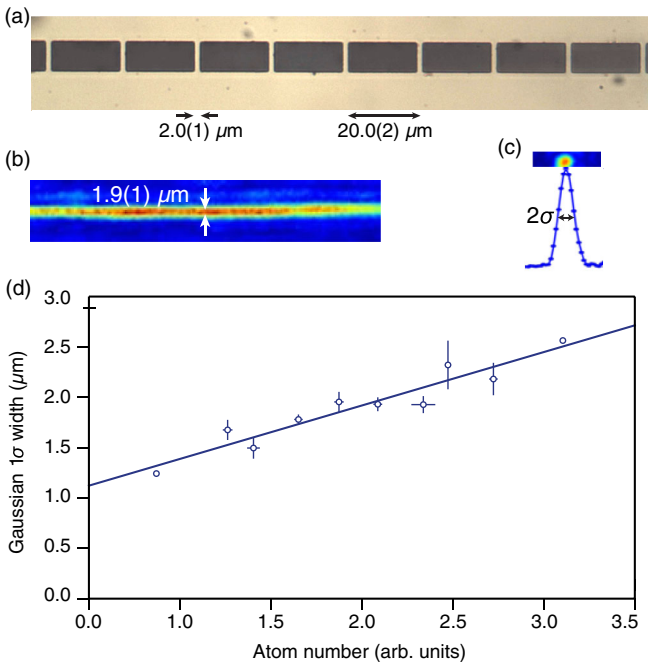

FIG. 12. Resolution measurement with the 2-μm wire. (a) Image of $2.0(1)$-μm microwires spaced $20.0(2)$ μm apart. (b) Measurement of resolution in $\hat{z}$ using transverse width of unfragmented BEC (i.e., zero current flowing in the calibration wire). The FWHM shown between the white arrows is $1.9(1)$ μm. (c) Image of one dot of the fragmented BEC in the potential of the microwires. A Gaussian is fit to determine spot size; the 2σ width is indicated by the black arrows. (d) Resolution versus atom number as measured by fits such as that in panel (c). The y intercept is $1.1(1)$ μm.

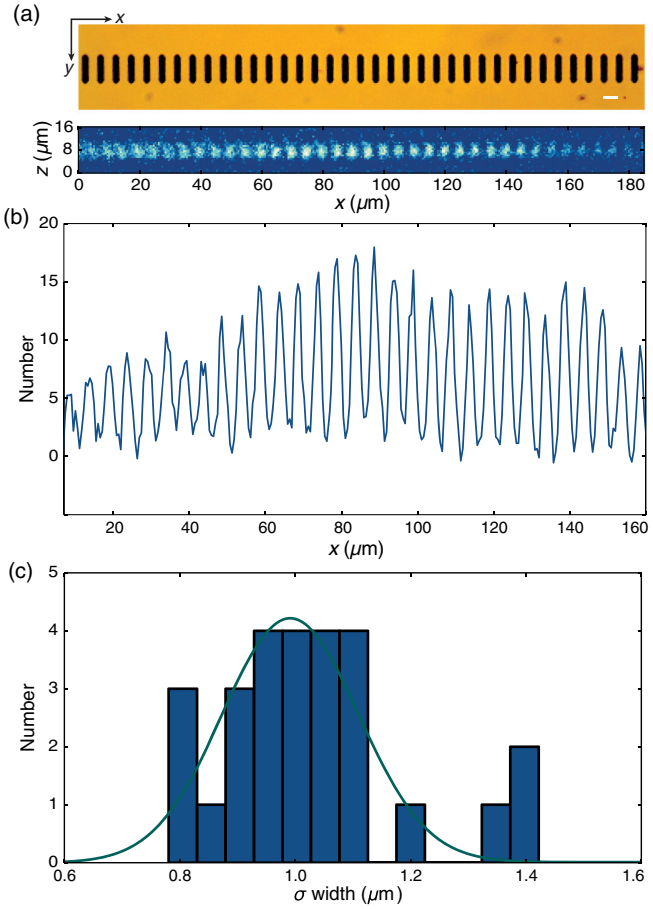

FIG. 13. Resolution measurements with an array of 2.5-μm wires. (a) Microwire array used for the resolution measurement. Wires are 2.5 μm wide, 2.5 μm spaced, and 10 μm long. (b) Number of atoms per pixel along $\hat{x}$ integrated along the $\hat{z}$ direction. (c) Result of Gaussian fit to each peak in panel (b). The histogram displays the 1σ widths of each of these peaks, and the green Gaussian is a fit to this distribution of widths. The mean width is $1.0(1)$ μm, providing a FWHM resolution estimate of $2.4(2)$ μm.

weighted averages [53] of the measurements to obtain the SQCRAMscope atom density and field FWHM resolvability of 2.2(1) μm.

The resolvability of current sources a distance d away from the *in situ* gas position is reduced by the convolution of the field resolvability with the field propagation transfer function, i.e., the Biot-Savart Green's function we describe below. For a wire with transverse dimensions much smaller than d, the current path resolvability is $\sqrt{\sigma_r^2 + d^2} = 2.3(1)$ μm for a BEC distance $d = 0.8(1)$ μm, or 2.8(1) μm at $d = 1.7(1)$ μm away.

APPENDIX C: FIELD-SENSING CALIBRATIONS

1. Field-to-current mapping

The mapping from measured field to inferred current distribution is performed using the procedure outlined in Ref. [54] and also employed in Refs. [6–8,55]. Using a Green's function that accounts for the finite thickness of the source wires, the Biot-Savart mapping between field and current is

$$j_y(k_x, k_y) = \frac{\bar{k} b_x(k_x, k_y, d)}{\mu_0 \sinh(\bar{k}h/2)} e^{\bar{k}(d+h/2)}, \tag{C1}$$

$$j_x(k_x, k_y) = -\frac{k_y}{k_x} j_y(k_x, k_y), \tag{C2}$$

where j_i is the current density in a wire of thickness h, and $\bar{k} = \sqrt{k_x^2 + k_y^2}$ is the spatial wave number. The measured $B_x(x, y)$-field map taken at d is first Fourier transformed with a spatial fast Fourier transform (FFT) algorithm. Then, $b_x(k_x, k_y, d)$ is filtered with the Green's function effecting the Biot-Savart mapping from field-to-source current at a distance d, i.e., applying Eq. (C1). A Hanning window is numerically applied to the current density $j_y(k_x, k_y)$ to remove spurious high spatial frequencies. Equation (C2) yields $j_x(k_x, k_y)$, and finally an inverse FFT algorithm provides $J_x(x, y)$ and $J_y(x, y)$.

2. Accuracy of extended-dynamic-range trap

We measure the accuracy, linearity, and dynamic range of the extended-dynamic-range trap in a manner similar to that presented in Fig. 3. The data are plotted in Fig. 14, where the green line is the fit to the linear region and has a slope 0.65(5). This implies a 3×-worse accuracy than the high-sensitivity trap, possibly because it operates closer to the limit of the quasicondensate regime. As for the data in Fig. 3, we use a calibrated current source for generating the microwire current. From this slope, we find that the responsivity is 35(5)% lower than the expected $R = 4.81(8)$ nT/(atom/μm) for this trap.

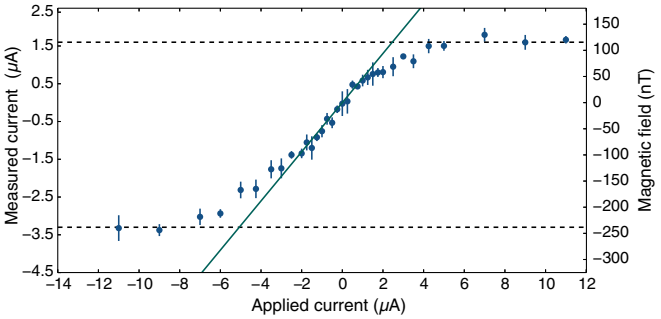

FIG. 14. Accuracy of the extended-dynamic-range trap. Measurement of current in the 6-μm-wide gold calibration wire. BEC is positioned 1.3(4) μm below the wire center using the extended-dynamic-range trap, and the current is varied to create a density dimple or peak in the atomic density. The green line is a fit to the linear region.

3. Imaging noise

Noise contributions in the three images arise from the noise of the resonant laser beam as well as electronic readout and dark counts from the CCD camera. We measure the per-pixel noise by performing absorption imaging without atoms present. We care about the noise in a single image, and so rather than record the shot-by-shot statistics of counts in one pixel, which includes an irrelevant contribution from laser intensity noise, we use the inhomogeneous imaging light intensity across the pixel array to measure the statistics of a single-shot image. Each pixel of the image is binned by the mean photon number, and the variance versus mean of the number of counts in each bin is plotted in Fig. 15(a). The line of unity slope represents the photon shot-noise limit. For short exposure times, the chilled CCD camera exhibits only 0.07 counts/pixel/s of dark count noise, but the readout contributes $\sigma = 4.59(2)$ counts/pixel during our imaging time, as measured by examining the count statistics of the dark image taken during absorption imaging; see Fig. 15(b). This readout noise dominates over shot noise below approximately five counts per pixel. We observe that the imaging system is shot-noise limited between approximately 100 and 3600 counts per pixel. The high-sensitivity trap is operated at 3000 counts per pixel, contributing to an equivalent field noise of 2.5(4) nT, which is consistent with the expected photon shot noise of 2.2 nT. In order to stay within the strongly saturated regime of atomic scattering, the extended-dynamic-range trap, which confines atoms at higher peak atomic density, is operated at 4500 counts per pixel.

4. Atom noise

Images of the BECs contain atomic density noise in addition to photon shot noise, and the atomic density noise can come from both shot-to-shot variance in the total

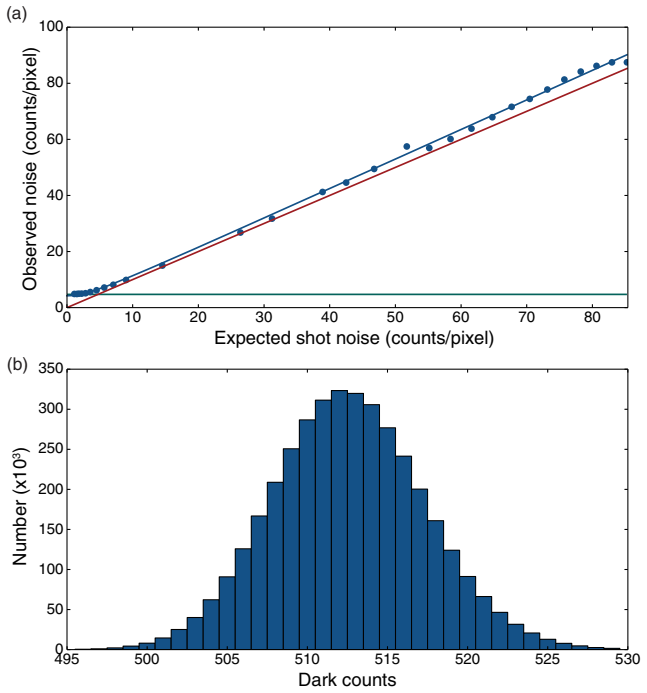

FIG. 15. Imaging noise measurement. (a) Observed noise per pixel versus expected photon shot-noise per pixel. Below approximately 3600 counts per pixel (60 expected noise counts), the noise (blue data) is nearly at the expected photon shot-noise limit (red line). But below approximately 25 counts per pixel (five expected noise counts), the noise is dominated by readout noise of the CCD. The green line shows the contribution due to these fluctuations. We measure this level using the reference dark images taken during absorption imaging. The blue line is a fit to the data. (b) Histogram of photon counts in each pixel of the dark image, with a Gaussian fit of $\sigma = 4.68(2)$ counts from the readout noise.

trapped atom number as well as intrinsic atomic density fluctuations from position to position along the quasicondensate. The variance in the total atom number is recorded in each shot and accurately accounted for in each run's density-to-field mapping as long as the quasicondensate equation of state remains valid. However, the pixel-by-pixel density fluctuation does contribute to the noise floor. To eliminate the contribution of total trap population fluctuations to the measurement of the intrinsic atom density noise, we compare the pixel-by-pixel density of a single-shot image to the mean density in each pixel expected for the gas, where we define a pixel to mean the $\hat{z}$-integrated atomic density. This comparison is accomplished by fitting the imaged density profile to a quasicondensate profile [11] for the same total atom number and trap parameters. This provides a mean and residual atom number for each pixel of this image, and we repeat this procedure for many such images. We then bin the means and find the residual variance for each mean. These are plotted in Fig. 16, where the black lines are the atom shot-noise limits for two

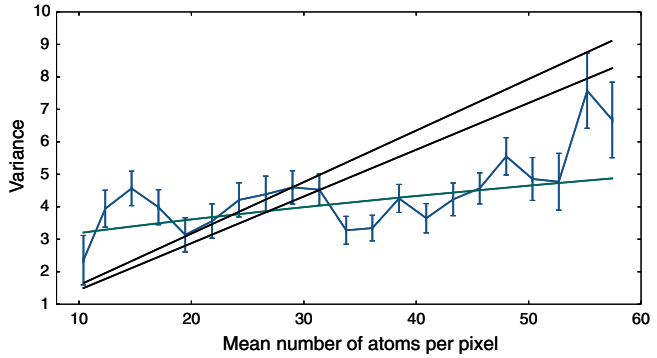

FIG. 16. Atom noise measurement. Variance versus mean atom number per pixel in images of quasi-1D BEC density. The data with photon shot noise subtracted are fit to expressions from Ref. [11] and result in the green curve. The black lines correspond to the atom shot-noise limit (unity slope) for imagining resolutions of 2.2 μm (top black line) and 2.5 μm (bottom black line).

imaging resolutions. The green line is the fit to the data using expressions from Ref. [11] for a quasicondensate. The fit allows us to measure the temperature of the gas [11,13], which is otherwise difficult to do given the short TOF permitted by our imaging system and the small number of atoms in the thermal wings at this temperature.

We see that the atom noise is sub-Poissonian for atom numbers per pixel above 30. The sub-shot-noise atom noise statistics are indicative of a quasicondensate, as discussed in Ref. [13]. We operate the experiment such that the majority of pixels contain atoms in the 30–50 per-pixel range. Mean atom numbers below 10 correspond to regions of the gas not described by the quasi-1D equation of state, either because these are thermal atoms pushed out from the center of the gas into the wings [56] and/or because this is the region in which the validity of Thomas-Fermi approximation breaks down. As such, these regions are not used for magnetometry, while numbers above 57 correspond to small regions around the centers of unusually dense BECs, leading to worse statistics in the figure. The average atom noise is 1.7(7) nT, slightly less than that from photon shot noise.

The atom shot-noise limits differ from unity slope due to the artificial averaging of fluctuations [57]. This deviation is caused by the blurring due to finite imaging resolution, expansion during the short TOF, and atom diffusion arising from the random recoil imparted during imaging. The diffusion spot size is known to be accurately modeled by the diffusion equation $r_{\mathrm{rms}} = \sqrt{N v_r^2 \Delta t^2/3} \propto t^{3/2}$, where N is the number of photons scattered, and $v_r = 5.88$ mm/s is the recoil velocity on the imaging transition [50]. The value of r_{rms} is approximately 530 nm for our parameters. This is included in the measurements of the imaging resolution. Accounting for these effects, we obtain the two shot-noise limits in Fig. 16 associated with imaging resolutions between 2.2 and 2.5 μm.

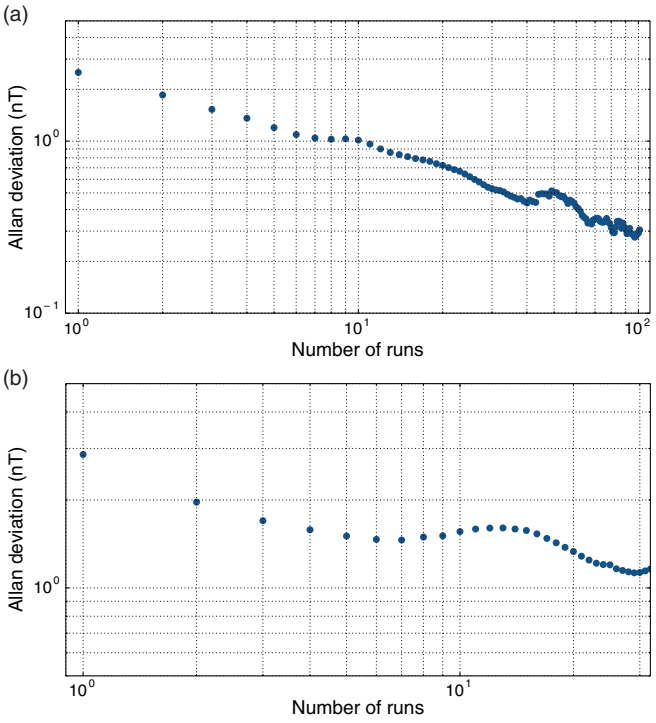

FIG. 17. Magnetometry stability. (a) Allan deviation of the minimum detectable field. Noise floor is approximately 300 pT per pixel (no spatial averaging) after 100 runs of the experiment. (b) Allan deviation of the repeatability of measurements of the 30-nT field generated by current running though the 12-μm-wide wire used in the accuracy measurements presented in Fig. 3. The stability in the repeatability of the field is approximately 1.1 nT after 30 runs.

5. Allan deviation

We measure the stability of the magnetometer using two methods. In Fig. 17(a), we present a measurement of the Allan deviation of the minimum detectable field above the same 12-μm-wide wire used for the accuracy measurements in Fig. 3 without current running in the wire. This field has a noise floor of approximately 300 pT per pixel (no averaging) after 100 runs of the experiment, which takes roughly half an hour, though we collect information on approximately 100 pixels during this time and, thus, spend less than 20 s per pixel. In the second measurement, we investigate the Allan deviation of the repeatability of the measurements of the 30-nT field created by flowing 750 nA through the 12-μm-wide wire with the atoms trapped 1.2 μm below. The stability of the field is approximately 1.1 nT after 30 runs. The factors that may contribute to this minimum stability level are the residual sloshing of the motion of the BEC within the trap and the drift of the position of the BEC relative to the sample.

6. Patch fields

Our SQCRAMscope is sensitive to other forces from the sample surface besides magnetic fields. With BECs trapped in atom chips near surfaces, Casimir-Polder forces have been detected [22,23] and used to determine the position of carbon nanotubes [58]. Electric fields from surface charges can be detected [7]. Such fields may arise from adsorbed Rb atoms, which can pose a difficulty for various applications [39,59–66]. The electric field is due to an induced dipole whose magnitude varies depending on the surface properties. The force increases as more atoms are absorbed onto the surface, which may occur as atoms escape the atom-chip trap during loading, rf evaporation, or during TOF expansion.

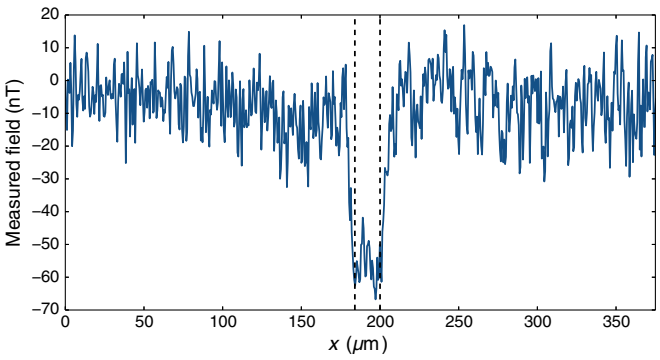

FIG. 18. Patch-field measurement. Measured fictitious magnetic field 1.4(3) μm from the sample due to a patch potential on the 16-μm microwire. This potential arises after a BEC is created approximately 1000 times within a few microns below the array. Black dashed lines indicate the positions of the wire edges.

Indeed, we observe an electric force on the atoms once we create a BEC below a particular place below the calibration chip more than 1000 times. The effects vanish once we move the BEC a few tens of microns to a fresh location. Figure 18 shows this effect after approximately 1000 repetitions with a BEC positioned approximately 1 μm from a room-temperature, 16-μm-wide gold wire. The wire is 400 nm taller than the surrounding silicon substrate, and so the electric field from the adatoms on the surface of the wire dominates that from the substrate to either side.

The electric field from the adsorbed atoms creates a local potential above the wire. This is due to several effects: (1) the closer proximity of the Au to the atoms than the Si, (2) the different polarizabilities of Rb on Au versus Si, and (3) the potentially different adhesion characteristics of Rb to Au versus Si. This potential reduces the magnetometer's dynamic range and increases its sensitivity to sample height fluctuations.

We do not expect this patch-field effect to play a deleterious role in future SQCRAMscope magnetometry experiments because (1) most samples will have a smooth surface of a homogeneous material, reducing the force on the atoms from electric field gradients to a negligible level, (2) samples can be on the millimeter scale, allowing the use of fresh portions of the sample when needed, and (3) fresh

samples may be introduced with minimal downtime. Nevertheless, we can investigate the efficacy of various methods for adatom removal that have been tried by other groups, including sample heating, laser ablation and UV-light desorption [39,59–66].

[1] M. S. Grinolds, S. Hong, P. Maletinsky, L. Luan, M. D. Lukin, R. L. Walsworth, and A Yacoby, Nanoscale magnetic imaging of a single electron spin under ambient conditions, Nat. Phys. **9**, 215 (2013).

[2] D. Vasyukov, Y. Anahory, L. Embon, D. Halbertal, J. Cuppens, L. Neeman, A. Finkler, Y. Segev, Y. Myasoedov, M. L. Rappaport, M. E. Huber, and E. Zeldov, A scanning superconducting quantum interference device with single electron spin sensitivity, Nat. Nanotechnol. **8**, 639 (2013).

[3] J. R. Kirtley, L. Paulius, A. J Rosenberg, J. C. Palmstrom, C. M. Holland, E. M. Spanton, D. Schiessl, C. L. Jermain, J. Gibbons, Y. K. K. Fung, M. E. Huber, D. C. Ralph, M. B. Ketchen, G. W. Gibson, Jr., and K. A. Moler, Scanning SQUID susceptometers with sub-micron spatial resolution, Rev. Sci. Instrum. **87**, 093702 (2016).

[4] J. Estève, C. Aussibal, T. Schumm, C. Figl, D. Mailly, I. Bouchoule, C. I. Westbrook, and A. Aspect, Role of wire imperfections in micromagnetic traps for atoms, Phys. Rev. A **70**, 043629 (2004).

[5] A. Günther, M. Kemmler, S. Kraft, C. J. Vale, C. Zimmermann, and J. Fortágh, Combined chips for atom optics, Phys. Rev. A **71**, 063619 (2005).

[6] S. Wildermuth, S. Hofferberth, I. Lesanovsky, E. Haller, L. Mauritz Andersson, S. Groth, I. Bar-Joseph, P. Krüger, and J. Schmiedmayer, Bose-Einstein condensates—Microscopic magnetic-field imaging, Nature (London) **435**, 440 (2005).

[7] S. Wildermuth, S. Hofferberth, I. Lesanovsky, S. Groth, P. Krüger, J. Schmiedmayer, and I. Bar-Joseph, Sensing electric and magnetic fields with Bose-Einstein condensates, Appl. Phys. Lett. **88**, 264103 (2006).

[8] S. Aigner, L. Della Pietra, Y. Japha, O. Entin-Wohlman, T. David, R. Salem, R. Folman, and J. Schmiedmayer, Long-range order in electronic transport through disordered metal films, Science **319**, 1226 (2008).

[9] J. Fortágh and C. Zimmermann, Magnetic microtraps for ultracold atoms, Rev. Mod. Phys. **79**, 235 (2007).

[10] M. A. Naides, R. W. Turner, R. A. Lai, J. M. DiSciacca, and B. L. Lev, Trapping ultracold gases near cryogenic materials with rapid reconfigurability, Appl. Phys. Lett. **103**, 251112 (2013).

[11] F. Gerbier, Quasi-1D Bose-Einstein condensates in the dimensional crossover regime, Europhys. Lett. **66**, 771 (2004).

[12] I. Bloch, J. Dalibard, and W. Zwerger, Many-body physics with ultracold gases, Rev. Mod. Phys. **80**, 885 (2008).

[13] T. Jacqmin, J. Armijo, T. Berrada, K. V. Kheruntsyan, and I. Bouchoule, Sub-Poissonian Fluctuations in a 1D Bose Gas: From the Quantum Quasicondensate to the Strongly Interacting Regime, Phys. Rev. Lett. **106**, 230405 (2011).

[14] We actually employ the full expression given in Ref. [11]; see, also, Ref. [15].

[15] P. Krüger, S. Hofferberth, I. E. Mazets, I. Lesanovsky, and J. Schmiedmayer, Weakly Interacting Bose Gas in the One-Dimensional Limit, Phys. Rev. Lett. **105**, 265302 (2010).

[16] J.-H. Chu, J. G. Analytis, K. De Greve, P. L. McMahon, Z. Islam, Y. Yamamoto, and I. R. Fisher, In-plane resistivity anisotropy in an underdoped iron arsenide superconductor, Science **329**, 824 (2010).

[17] J. A. Bert, B. Kalisky, C. Bell, M. Kim, Y. Hikita, H. Y. Hwang, and K. A. Moler, Direct imaging of the coexistence of ferromagnetism and superconductivity at the $LaAlO_3$/$SrTiO_3$ interface, Nat. Phys. **7**, 767 (2011).

[18] M. M. Qazilbash, M. Brehm, B.-G. Chae, P. C. Ho, G. O. Andreev, B.-J. Kim, S. J. Yun, A. V. Balatsky, M. B. Maple, F. Keilmann, H.-T. Kim, and D. N. Basov, Mott transition in VO_2 revealed by infrared spectroscopy and nano-imaging, Science **318**, 1750 (2007).

[19] B. Dellabetta, T. L. Hughes, M. J. Gilbert, and B. L. Lev, Imaging topologically protected transport with quantum degenerate gases, Phys. Rev. B **85**, 205442 (2012).

[20] K. C. Nowack, E. M. Spanton, M. Baenninger, M. König, J. R. Kirtley, B. Kalisky, C. Ames, P. Leubner, C. Brüne, H. Buhmann, L. W. Molenkamp, D. Goldhaber-Gordon, and K. A. Moler, Imaging currents in HgTe quantum wells in the quantum spin Hall regime, Nat. Mater. **12**, 787 (2013).

[21] J. Zaanen, Electrons go with the flow in exotic material systems, Science **351**, 1026 (2016).

[22] Y.-j. Lin, I. Teper, C. Chin, and V. Vuletić, Impact of the Casimir-Polder Potential and Johnson Noise on Bose-Einstein Condensate Stability near Surfaces, Phys. Rev. Lett. **92**, 050404 (2004).

[23] J. M. Obrecht, R. J. Wild, M. Antezza, L. P. Pitaevskii, S. Stringari, and E. A. Cornell, Measurement of the Temperature Dependence of the Casimir-Polder Force, Phys. Rev. Lett. **98**, 063201 (2007).

[24] J. R. Kirtley, B. Kalisky, J. A. Bert, C. Bell, M. Kim, Y. Hikita, H. Y. Hwang, J. H. Ngai, Y. Segal, F. J. Walker, C. H. Ahn, and K. A. Moler, Scanning SQUID susceptometry of a paramagnetic superconductor, Phys. Rev. B **85**, 224518 (2012).

[25] M. Iranmanesh, M. Stir, J. R. Kirtley, and J. Hulliger, Scanning SQUID microscopy of local superconductivity in inhomogeneous combinatorial ceramics, Chem. Eur. J. **20**, 15816 (2014).

[26] L. M. Pham, D. Le Sage, P. L. Stanwix, T. K. Yeung, D. Glenn, A. Trifonov, P. Cappellaro, P. R. Hemmer, M. D. Lukin, H. Park, A. Yacoby, and R. L. Walsworth, Magnetic field imaging with nitrogen-vacancy ensembles, New J. Phys. **13**, 045021 (2011).

[27] B. J. Shields, Q. P. Unterreithmeier, N. P. de Leon, H. Park, and M. D. Lukin, Efficient Readout of a Single Spin State in Diamond via Spin-to-Charge Conversion, Phys. Rev. Lett. **114**, 136402 (2015).

[28] I. Lovchinsky, A. O. Sushkov, E. Urbach, N. P. de Leon, S. Choi, K. De Greve, R. Evans, R. Gertner, E. Bersin, C. Müller, L. McGuinness, F. Jelezko, R. L. Walsworth, H. Park, and M. D. Lukin, Nuclear magnetic resonance detection and spectroscopy of single proteins using quantum logic, Science **351**, 836 (2016).

[29] M. Vengalattore, J. M. Higbie, S. R. Leslie, J. Guzman, L. E. Sadler, and D. M. Stamper-Kurn, High-Resolution

Magnetometry with a Spinor Bose-Einstein Condensate, Phys. Rev. Lett. **98**, 200801 (2007).
[30] A. J. Brook, S. J. Bending, J. Pinto, A. Oral, D. Ritchie, H. Beere, M. Henini, and A. Springthorpe, Integrated piezoresistive sensors for atomic force-guided scanning Hall probe microscopy, Appl. Phys. Lett. **82**, 3538 (2003).
[31] T. Nirrengarten, A. Qarry, C. Roux, A. Emmert, G. Nogues, M. Brune, J. M. Raimond, and S. Haroche, Realization of a Superconducting Atom Chip, Phys. Rev. Lett. **97**, 200405 (2006).
[32] T. Mukai, C. Hufnagel, A. Kasper, T. Meno, A. Tsukada, K. Semba, and F. Shimizu, Persistent Supercurrent Atom Chip, Phys. Rev. Lett. **98**, 260407 (2007).
[33] C. Roux, A. Emmert, A. Lupascu, T. Nirrengarten, G. Nogues, M. Brune, J. M. Raimond, and S. Haroche, Bose-Einstein condensation on a superconducting atom chip, Europhys. Lett. **81**, 56004 (2008).
[34] T. Müller, B. Zhang, R. Fermani, K. S. Chan, Z. W. Wang, C. B. Zhang, M. J. Lim, and R. Dumke, Trapping of ultracold atoms with the magnetic field of vortices in a thin-film superconducting micro-structure, New J. Phys. **12**, 043016 (2010).
[35] J. Reichel and V. Vuletic, *Atom Chips* (Wiley, New York, 2010).
[36] D. Cano, B. Kasch, H. Hattermann, R. Kleiner, C. Zimmermann, D. Koelle, and J. Fortágh, Meissner Effect in Superconducting Microtraps, Phys. Rev. Lett. **101**, 183006 (2008).
[37] F. Jessen, M. Knufinke, S. C. Bell, P. Vergien, H. Hattermann, P. Weiss, M. Rudolph, M. Reinschmidt, K. Meyer, T. Gaber, D. Cano, A. Günther, S. Bernon, D. Koelle, R. Kleiner, and J. Fortágh, Trapping of ultracold atoms in a 3He/4He dilution refrigerator, Appl. Phys. B **116**, 665 (2014).
[38] S. Minniberger, F. Diorico, S. Haslinger, C. Hufnagel, C. Novotny, N. Lippok, J. Majer, C. Koller, S. Schneider, and J. Schmiedmayer, Magnetic conveyor belt transport of ultracold atoms to a superconducting atomchip, Appl. Phys. B **116**, 1017 (2014).
[39] K. S. Chan, M. Siercke, C. Hufnagel, and R. Dumke, Adsorbate Electric Fields on a Cryogenic Atom Chip, Phys. Rev. Lett. **112**, 026101 (2014).
[40] D. Rugar, R. Budakian, H. J. Mamin, and B. W. Chui, Single spin detection by magnetic resonance force microscopy, Nature (London) **430**, 329 (2004).
[41] C. F. Ockeloen, R. Schmied, M. F. Riedel, and P. Treutlein, Quantum Metrology with a Scanning Probe Atom Interferometer, Phys. Rev. Lett. **111**, 143001 (2013).
[42] S. Wildermuth, Ph.D. thesis, University of Heidelberg, 2005.
[43] S. Aigner, Ph.D. thesis, University of Heidelberg, 2007.
[44] M. Pelliccione, A. Jenkins, P. Ovartchaiyapong, C. Reetz, E. Emmanouilidou, N. Ni, and A. C. Bleszynski Jayich, Scanned probe imaging of nanoscale magnetism at cryogenic temperatures with a single-spin quantum sensor, Nat. Nanotechnol. **11**, 700 (2016).
[45] J. M. Taylor, P. Cappellaro, L. Childress, L. Jiang, D. Budker, P. R. Hemmer, A. Yacoby, R. Walsworth, and M. D. Lukin, High-sensitivity diamond magnetometer with nanoscale resolution, Nat. Phys. **4**, 810 (2008).
[46] P. Treutlein, P. Hommelhoff, T. Steinmetz, T. W. Hänsch, and J. Reichel, Coherence in Microchip Traps, Phys. Rev. Lett. **92**, 203005 (2004).
[47] E. Berg, E. Fradkin, E. A. Kim, S. A. Kivelson, V. Oganesyan, J. M. Tranquada, and S. C. Zhang, Dynamical Layer Decoupling in a Stripe-Ordered High-T_c Superconductor, Phys. Rev. Lett. **99**, 127003 (2007).
[48] E. Berg, E. Fradkin, and S. A. Kivelson, Theory of the striped superconductor, Phys. Rev. B **79**, 064515 (2009).
[49] S. Kivelson (private communication).
[50] W. Ketterle, D. S. Durfee, and D. M. Stamper-Kurn, in *Proceedings of the International School of Physics "Enrico Fermi", Course CXL*, edited by M. Inguscio, S. Stringari, and C. E. Wieman (IOS Press, Amsterdam, 1999), p. 67.
[51] D. A. Smith, S. Aigner, S. Hofferberth, M. Gring, M. Andersson, S. Wildermuth, P. Krüger, S. Schneider, T. Schumm, and J. Schmiedmayer, Absorption imaging of ultracold atoms on atom chips, Opt. Express **19**, 8471 (2011).
[52] G. Reinaudi, T. Lahaye, Z. Wang, and D. Guéry-Odelin, Strong saturation absorption imaging of dense clouds of ultracold atoms, Opt. Lett. **32**, 3143 (2007).
[53] R. C. Paule and J. Mandel, Consensus values and weighting factors, J. Res. Natl. Bur. Stand. **87**, 377 (1982).
[54] B. J. Roth, N. G. Sepulveda, and J. P. Wikswo, Jr., Using a magnetometer to image a two-dimensional current distribution, J. Appl. Phys. **65**, 361 (1989).
[55] L. Della Pietra, S. Aigner, C. vom Hagen, S. Groth, I. Bar-Joseph, H. J. Lezec, and J. Schmiedmayer, Designing potentials by sculpturing wires, Phys. Rev. A **75**, 063604 (2007).
[56] A. Griffin, T. Nikuni, and E. Zaremba, *Bose-Condensed Gases at Finite Temperatures* (Cambridge University Press, Cambridge, England, 2009).
[57] C.-L. Hung, X. Zhang, L.-C. Ha, S.-K. Tung, N. Gemelke, and C. Chin, Extracting density–density correlations from *in situ* images of atomic quantum gases, New J. Phys. **13**, 075019 (2011).
[58] M. Gierling, P. Schneeweiss, G. Visanescu, P. Federsel, M. Häffner, D. P. Kern, T. E. Judd, A. Günther, and J. Fortágh, Cold-atom scanning probe microscopy, Nat. Nanotechnol. **6**, 446 (2011).
[59] J. M. McGuirk, D. M. Harber, J. M. Obrecht, and E. A. Cornell, Alkali-metal adsorbate polarization on conducting and insulating surfaces probed with Bose-Einstein condensates, Phys. Rev. A **69**, 062905 (2004).
[60] J. M. Obrecht, R. J. Wild, and E. A. Cornell, Measuring electric fields from surface contaminants with neutral atoms, Phys. Rev. A **75**, 062903 (2007).
[61] H. Hattermann, M. Mack, F. Karlewski, F. Jessen, D. Cano, and J. Fortágh, Detrimental adsorbate fields in experiments with cold Rydberg gases near surfaces, Phys. Rev. A **86**, 022511 (2012).
[62] J. D. Carter, O. Cherry, and J. D. D. Martin, Electric-field sensing near the surface microstructure of an atom chip using cold Rydberg atoms, Phys. Rev. A **86**, 053401 (2012).
[63] H. Fan, S. Kumar, J. Sedlacek, H. Kübler, S. Karimkashi, and J. P. Shaffer, Atom based RF electric field sensing, J. Phys. B **48**, 202001 (2015).

[64] T. Thiele, J. Deiglmayr, M. Stammeier, J. A. Agner, H. Schmutz, F. Merkt, and A. Wallraff, Imaging electric fields in the vicinity of cryogenic surfaces using Rydberg atoms, Phys. Rev. A **92**, 063425 (2015).

[65] J. A. Sedlacek, E. Kim, S. T. Rittenhouse, P. F. Weck, H. R. Sadeghpour, and J. P. Shaffer, Electric Field Cancellation on Quartz by Rb Adsorbate-Induced Negative Electron Affinity, Phys. Rev. Lett. **116**, 133201 (2016).

[66] J. Naber, S. Machluf, L. Torralbo-Campo, M. L. Soudijn, N. J. van Druten, H. B. van Linden van den Heuvell, and R. J. C. Spreeuw, Adsorbate dynamics on a silica-coated gold surface measured by Rydberg Stark spectroscopy, J. Phys. B **49**, 094005 (2016).